Research Square

Preprints are preliminary reports that have not undergone peer review.
They should not be considered conclusive, used to inform clinical practice,
or referenced by the media as validated information.

Impact of Cover-Management Factor Estimation Methods on RUSLE-Based Soil Erosion and Sediment Yield in the Gilgel Abay Catchment, Lake Tana Basin, Northwestern Ethiopia

BALABATHINA VEERA NARAYANA

veeraa.geo@gmail.com

Department of Earth Sciences, Natural & Computational Sciences, University of Gondar, P.O. Box 196, Gondar, Ethiopia, East Africa. https://orcid.org/0000-0003-3202-2370

Research Article

Keywords: RUSLE, cover-management factor (C-factor), sediment delivery ratio, NDVI, Gilgel Abay catchment, Lake Tana

Posted Date: November 23rd, 2026

DOI: https://doi.org/10.21203/rs.3.rs-11319207/v1

License: This work is licensed under a Creative Commons Attribution 4.0 International License.
Read Full License

Impact of Cover-Management Factor Estimation Methods on RUSLE-Based Soil Erosion and Sediment Yield in the Gilgel Abay Catchment, Lake Tana Basin, Northwestern Ethiopia

Balabathina Veera Narayana*

* Department of Earth Sciences, Natural & Computational Sciences, University of Gondar, P.O. Box 196, Gondar, Ethiopia, East Africa.

Correspondence: veeraa.geo@gmail.com

Abstract

Soil erosion and sediment yield in the Gilgel Abay catchment (1,652 km²), a major sediment source for Lake Tana, are strongly influenced by the cover-management (C) factor in RUSLE modelling. However, previous studies have relied on single C-factor derivation methods without benchmarking against observed sediment yield. This study compares five C-factor methods: a literature-based scenario using Hurni's (1985) Ethiopian highland classification, a field-calibrated regression based on 88 ground-truth plots, and three NDVI-based formulations (linear, exponential, and precipitation-corrected) within a unified RUSLE framework. Resulting soil-loss and sediment-yield estimates were evaluated against suspended-sediment records from Bikolo and Chimba stations (2012–2016) using three independent sediment-delivery-ratio (SDR) formulations. A twelve-class land-use/land-cover map (overall accuracy 86.41%, Kappa = 0.8516) supported all scenarios. Annual soil loss varied more than threefold, from 11.89 million t yr^{-1} under field-calibrated regression to 37.79 million t yr^{-1} under exponential NDVI. Areas exceeding 50 t ha^{-1} yr^{-1} occupied 18.1% of the catchment but contributed 66.2% of total modelled soil loss. Across fifteen model–SDR combinations, sediment yield ranged from 1.31 to 7.67 million t yr^{-1}, compared with the observed benchmark of 3.21 million t yr^{-1}. Although no method consistently matched observations across all SDR formulations, field-calibrated regression achieved strong agreement with field-observed C-values (R^2 = 0.923). Findings demonstrate that C-factor selection and SDR formulation jointly govern model reliability, supporting locally validated methods and targeted conservation interventions in high-erosion sub-catchments.

Keywords: RUSLE; cover-management factor (C-factor); sediment delivery ratio; NDVI; Gilgel Abay catchment; Lake Tana

1. Introduction

Soil erosion is a pervasive form of land degradation with serious consequences for environmental sustainability, water resources, and agricultural productivity worldwide (Panagos et al. 2023). It removes tens of billions of tonnes of topsoil globally each year, degrading soil fertility, disrupting carbon and nutrient cycling, and accelerating reservoir sedimentation, with direct consequences for food security and hydropower generation in developing economies (Borrelli et al. 2023). The problem is particularly acute in regions with fragile topography and limited conservation infrastructure, such as the Ethiopian Highlands,

where steep slopes, intense rainfall events, and land-use change accelerate soil loss and sedimentation of reservoirs (Taye et al. 2017; Zerihun et al. 2018).

Water-driven land degradation of this kind is increasingly understood not only as a soil-science problem but as a spatial one, and river and catchment erosion cannot be adequately assessed from soil-loss equations in isolation — it must be connected to advanced GIS and remote-sensing (RS) methods for land-cover mapping, drainage-network analysis, and sediment-transport modelling (Jabar et al. 2023a). Recent work continues to demonstrate that integrating GIS/RS with hydrological and erosion modelling substantially improves the identification of degradation hotspots, sediment sources, and water-management priorities at catchment scale (Sayl et al. 2026; Sayl 2019; Jabar et al. 2023b; AL-Somaydaii and Abdaljader 2024; Assaf et al. 2021; Yousefi et al. 2022). This body of work provides the spatial resolution and temporal repeatability that field-based erosion studies alone cannot achieve.

To quantify erosion processes and support management decisions, scholars have developed a variety of empirical and process-based models notably the Universal Soil Loss Equation (USLE), the Revised Universal Soil Loss Equation (RUSLE), the Water Erosion Prediction Project (WEPP), the Morgan–Morgan–Finney (MMF) model, EUROSEM, and SEMMED - each with different complexity, process representation, and data requirements (Karydas and Panagos 2016; Guzha et al. 2018; Morgan 2005). Among these, RUSLE is widely adopted for estimating long-term average annual soil loss because of its flexibility, relatively low data demands, and ease of spatial implementation within a GIS environment (Borrelli et al. 2023).

A central determinant of RUSLE and of related models such as MUSLE performance is the cover-management factor (C), which quantifies the degree to which vegetation cover and management practices reduce soil loss relative to bare, continuously tilled ground, with values ranging from near 0 (dense, permanent cover) to 1 (bare soil). Traditional approaches assign constant C-values to discrete land-use/land-cover (LULC) categories drawn from field experiments or published tables, but such tabular values are static, cannot capture intra-class variability in canopy density or seasonal phenology, and are often transferred uncritically between regions with different vegetation structure (Panagos et al. 2023; Panagos et al. 2015). To address these limitations, C-factors are increasingly derived from remotely sensed vegetation information at the pixel level (Borrelli et al. 2023). The most widely used approach relates the Normalized Difference Vegetation Index (NDVI) to C through empirical exponential or linear regression equations — most commonly the formulations of Van der Knijff et al. (2000) and Durigon et al. (2014) — which convert continuous NDVI values into a continuous C surface without requiring reclassification into discrete LULC categories. Beyond NDVI, other spectral indices have been proposed to improve C-factor estimation where NDVI saturates under dense canopy or is biased by soil background reflectance, topography, and phenological stage. These include the Soil-Adjusted Vegetation Index (SAVI) and its modified and transformed variants (MSAVI, TSAVI), which incorporate a soil-brightness correction term; the Difference Vegetation Index (DVI) and Green NDVI (GNDVI), more sensitive to canopy chlorophyll content; and indices developed for residue and senescence detection, such as the Normalized Difference Tillage Index (NDTI) and Normalized Difference Senescent Vegetation Index (NDSVI) (Felix et al. 2023; Vîrghileanu et al. 2026). Spectral-unmixing

techniques offer a further refinement, valuable in the mixed smallholder-agriculture landscapes typical of the Ethiopian highlands (Karydas and Panagos 2016; Ren et al. 2026).

Building on this framework, the present study derives the C-factor for the Gilgel Abay catchment through a comparative approach spanning literature-based, remote-sensing-based, and field-calibrated methods. Tabular C-values were assigned by LULC and management class, drawn primarily from experimental studies conducted within Ethiopian highland agro-ecosystems, principally Hurni's (1985) classification for Ethiopian highland agriculture and subsequent Ethiopia-specific regional studies; temperate-agriculture sources such as Wischmeier and Smith (1978) were used only where no regionally appropriate value existed for a given crop type, applied to a minority of classes. In parallel, continuous C-factor surfaces were generated from NDVI through the linear regression formulation of Durigon et al. (2014) and the exponential regression of Van der Knijff et al. (2000), and through a seasonally adjusted, precipitation-corrected approach combining the moisture-correction framework of Felix et al. (2023) with the scene-normalized rescaling of Macedo et al. (2021) together accounting explicitly for the influence of antecedent rainfall on vegetation reflectance and its downstream effect on the C-factor. A fifth, locally calibrated regression was developed directly from the catchment's own field data, relating 88 ground-truth C-factor observations to multi-date NDVI composites acquired across the study area. Each resulting C-factor surface was propagated through RUSLE to produce an independent soil-loss estimate, and the corresponding sediment yields — obtained via the sediment-delivery-ratio framework of Colman et al. (2018) — were compared against historical suspended-sediment records from the Bikolo and Chimba gauge stations. This design allows the reliability of each derivation method to be assessed empirically, rather than assumed, and reflects the catchment's underlying geological and pedological heterogeneity (Section 2), where the coexistence of Nitisols, Vertisols, and Luvisols developed over Tertiary volcanic sequences produces markedly different erosion responses that a single, static C-value cannot represent.

Existing RUSLE applications in the Lake Tana and wider Blue Nile region have typically relied on a single C-factor derivation method, most often NDVI-based regression applied in isolation (Balabathina et al. 2020; Mengie et al. 2019; Tsegaye and Bharti 2021), or on locally calibrated plot values developed for specific conservation structures (Taye et al. 2017; Belayneh et al. 2019). What remains largely untested in this setting is how this different derivation philosophies compare against one another, and, more importantly, against independently observed catchment sediment output. Addressing this gap, the present study compares five C-factor derivation methods within a single RUSLE framework and evaluates each against gauge-based sediment records, offering both an empirically grounded assessment of method reliability for this catchment and a transferable protocol applicable to other data-scarce highland systems where continuous, contemporaneous sediment monitoring is rarely available.

Accordingly, this study applies RUSLE to the Gilgel Abay catchment to examine how C-factor values derived from tabular, standard NDVI-regression, seasonally adjusted NDVI-regression, and locally calibrated NDVI-regression methods diverge across the catchment, how these differences propagate into RUSLE-predicted soil loss and sediment yield, and how the resulting patterns relate to the catchment's geology, soils, and land-use history. In doing so, the research

aims to move beyond method selection based on convention or convenience, toward an evidence-based basis for parameterizing RUSLE's C-factor in Ethiopian highland catchments and comparable settings elsewhere.

2. Study Area

The study was conducted in the Gilgel Abay catchment, which forms part of the Lake Tana sub-basin in the Upper Blue Nile River Basin, northwestern Ethiopia (Figure 1). Geographically, the catchment lies between approximately 36°45′E–37°15′E longitude and 10°00′N–11°30′N latitude, covering an estimated area of about 1,650 km². The Gilgel Abay River (also known as the Lesser Nile) is one of the major tributaries feeding Lake Tana, the largest lake in Ethiopia and the primary source of the Blue Nile River. The catchment is of strategic hydrological and ecological importance, influencing sediment delivery to the lake and downstream hydroelectric and irrigation schemes. The Gilgel Abay catchment exhibits a rugged and undulating topography, with elevations ranging from approximately 1,788 m to 3,534 m above sea level (Figure 1). The higher elevations are in the southern and southeastern parts, characterized by steep slopes and deeply dissected terrain, while the northern sections gradually flatten toward the lake. This marked altitudinal gradient strongly controls runoff velocity, erosion potential, and sediment transport dynamics. The region's topography, combined with intense seasonal rainfall, renders it highly susceptible to sheet, rill, and gully erosion, especially on cultivated slopes.

Climatically, the catchment experiences a tropical highland monsoon climate, governed primarily by the seasonal migration of the Intertropical Convergence Zone (ITCZ) (Dile et al. 2013). The area receives a mean annual rainfall of about 1,400–1,800 mm, with over 80% of the precipitation concentrated between June and September. The mean annual temperature ranges from 14°C in the highlands to about 25°C in the lower elevations near the lake. Such rainfall intensity and concentration during a short rainy period create conditions favourable for severe soil erosion and surface runoff generation (Bogale et al. 2020). The rainfall erosivity factor (R) in RUSLE applications for this region is therefore among the highest in the Blue Nile Basin (Balabathina et al. 2020). The Gilgel Abay River, the dominant drainage system of the catchment, originates in the southeastern highlands and flows northwest into Lake Tana. Numerous first- and second-order tributaries contribute to its flow, creating a dense dendritic drainage pattern. The river's discharge is highly seasonal, with peak flows corresponding to the main rainy season. The two primary hydrological monitoring stations, Bikolo (upper catchment) and Chimba (lower catchment), are crucial for validating sediment yield estimates and calibrating erosion models. Sediment transport from this catchment is a significant contributor to Lake Tana's siltation problem, adversely affecting water storage and aquatic habitats.

The catchment's soils are dominated by Nitisols, Vertisols, and Luvisols, which are moderately to highly susceptible to erosion depending on slope and land management. Nitisols, prevalent in the upper highlands, are deep and well-drained but prone to degradation under intensive cultivation. Vertisols occupy valley bottoms and gentle slopes, while Luvisols are found in the mid-slope transitional zones. Land use/land cover (LULC) is a mosaic of cultivated land,

grazing areas, shrubland, forest remnants, and settlement areas. Agriculture is predominantly rain-fed, with major crops including teff, maize, barley, and wheat. Over the past decades, rapid population growth and agricultural expansion have resulted in deforestation, vegetation degradation, and cultivation on marginal lands, which are major drivers of soil erosion (Andualem and Gebremariam 2015; Usman et al. 2023). Seasonal variations in vegetation cover make the C-factor highly dynamic, underscoring the need to test remote-sensing-based approaches for more accurate estimation. Geologically, the catchment is underlain mainly by Tertiary volcanic rocks, including basaltic and trachytic formations, interbedded with lacustrine sediments closer to Lake Tana (Gashaw et al. 2020). The weathering of these volcanic rocks has produced fertile but erosion-prone soils. The area's geomorphology reflects intense fluvial incision and tectonic uplift typical of the Ethiopian highlands, contributing to high slope gradients and variable soil depths that affect erosion modelling inputs such as the LS-factor in RUSLE.

The Gilgel Abay catchment is one of the most erosion-prone sub-catchments in the Lake Tana Basin. Excessive sediment inflow from this catchment contributes significantly to Lake Tana's siltation, reducing its ecological integrity and the efficiency of downstream hydropower and irrigation infrastructure (Alebachew et al. 2025). The complex interplay between topography, land management, and vegetation cover dynamics makes this catchment an ideal setting to examine the impact of C-factor estimation methods on soil erosion modelling accuracy, providing a valuable test site for improving RUSLE parameterization using both empirical and remote-sensing-based techniques.

3. Materials and Methods

3.1 Data Acquisition

The study relied on a comprehensive suite of spatial and temporal datasets to support the assessment of soil erosion and sediment yield. A Digital Elevation Model (DEM) was obtained from the ASTER Global Digital Elevation Model (GDEM) at 1 arc-second (~30 m) spatial resolution and used to characterize terrain attributes, generate hydrologically corrected flow-direction and flow-accumulation layers, and delineate the catchment boundary. Multi-temporal, orthorectified Landsat 8 OLI/TIRS imagery (Path 170, Row 52; 30 m spatial resolution) was acquired from the United States Geological Survey (USGS) EarthExplorer portal, covering the period March 2019–February 2020, with five representative scenes selected to capture pre-, peak-, and post-rainy-season conditions for a robust characterization of seasonal vegetation dynamics. Long-term daily rainfall records (1980–2020; 40 years) were compiled from 30 meteorological stations located within and surrounding the catchment to characterize long-term rainfall erosivity, while soil attribute data were obtained from two complementary sources, the Ethiopian Soil Information System (EthioSIS) and the Harmonized World Soil Database (HWSD, version 1.2; FAO). Where soil classification or attribute values (e.g., texture, depth, organic carbon) differed between the two sources for the same location, EthioSIS was treated as the primary source given its finer spatial resolution and direct calibration to Ethiopian field conditions, with HWSD used to supplement coverage in areas where EthioSIS data were unavailable. Land use/land cover (LULC) information was derived from existing reference

maps and validated through field observations across the catchment. All spatial data processing, analysis, and model implementation were carried out in ArcGIS 10.4 and ENVI 5.6, supplemented by HEC-GeoHMS and other relevant GIS extensions to ensure accurate integration and representation of the datasets described above.

3.2 Terrain Pre-processing and Catchment Delineation

The DEM was first pre-processed to ensure hydrologic consistency: sink cells were filled to obtain a hydrologically correct surface, and flow direction and flow accumulation rasters were generated. A pour point corresponding to the Gilgel Abay River outlet at Lake Tana was then specified. Using HEC-GeoHMS tools integrated within ArcGIS 10.4, the stream network was derived by selecting cells exceeding a defined flow accumulation threshold, and the catchment boundary was delineated by tracing upstream from the pour point. The processed DEM also enabled calculation of slope and aspect rasters, which fed into the computation of the LS (slope length and steepness) factor. The resulting stream network and drainage patterns provided the basis for mapping hydrologic response units and sediment delivery pathways.

3.3 Land Use/Land Cover (LULC) Mapping and Accuracy Assessment

To derive a current LULC map suitable for RUSLE input and C-factor attribution, the selected Landsat 8 images were radiometrically calibrated, atmospherically corrected using the FLAASH module in ENVI, and topographically normalized using solar azimuth and solar elevation to mitigate terrain-induced illumination differences. A two-stage classification approach was used: an initial unsupervised classification of NDVI and the original spectral bands yielded 50 and 40 spectral classes, respectively, which were subsequently aggregated into supervised classification schemes of 15 and 21 classes, respectively, guided by ground-truthing comprising approximately 20% aerial reconnaissance and ground survey of targeted plots. Problematic spectral classes, such as sisal, sparse lava flows, and young row crops, were addressed through post-classification refinement. The final LULC map achieved an overall classification accuracy of 86.41% (Kappa = 0.8516) after removal of topographic effects. Each LULC class was assigned a literature-based C-value (C_lit) drawn primarily from Hurni's (1985) Ethiopian highland classification, supplemented by locally calibrated values from regional studies for crop types not covered by Hurni; where neither source provided a suitable value, C-values were adopted from Wischmeier and Smith (1978) as a last-resort reference, applied to a minority of LULC classes only.

3.4 RUSLE Framework and Factor Computation

Soil-loss estimation was based on the Revised Universal Soil Loss Equation (RUSLE):

$$A = R \times K \times L \times S \times C \times P \qquad (1)$$

where A is the mean annual soil loss (t ha^{-1} yr^{-1}), R is the rainfall-runoff erosivity factor, K is the soil erodibility factor, L and S are the slope-length and slope-steepness factors, C is the cover-management factor, and P is the support-practice factor (Renard et al. 1997; Wischmeier and Smith 1978). Each factor was spatialized as a 30 m resolution raster layer and combined

through cell-by-cell multiplication in a GIS environment to generate the spatial distribution of A for each C-factor scenario.

3.4.1 Rainfall Erosivity Factor (R)

In the absence of high-resolution rainfall-intensity data, the R-factor was estimated using an empirical relationship developed for Ethiopian conditions (Hurni 1985):

$$R = 0.562P - 8.12 \quad (2)$$

where R is the rainfall erosivity factor ($MJ \cdot mm \cdot ha^{-1} \cdot h^{-1} \cdot yr^{-1}$) and P is the mean annual precipitation (mm). Using 40 years of daily rainfall data from 30 stations distributed within and surrounding the catchment, gridded precipitation surfaces were generated through spatial interpolation and subsequently converted to R using the empirical relationship above. The resulting R raster was validated against previously published regional R-values for comparable Ethiopian highland catchments.

3.4.2 Soil Erodibility Factor (K)

The K-factor ($t \cdot ha \cdot h \cdot ha^{-1} \cdot MJ^{-1} \cdot mm^{-1}$) quantifies the susceptibility of soil to erosion as a function of texture, organic matter content, structure, and permeability (Wischmeier and Smith 1978). Soil attribute data from EthioSIS and HWSD (v1.2) were processed to extract the parameters required for K-factor computation: the modified percent silt and percent sand fractions, organic matter content (a), soil structure code (b), and soil permeability class (c). The K-factor was computed as:

$$K = [2.1 \times 10^{-4} (12 - a) M^{1.14} + 3.25(b - 2) + 2.5(c - 3)] / 100 \quad (3)$$

where M is the product of the primary particle-size fractions [(% modified silt) × (% silt + % sand)], a is the percentage of organic matter, b is the soil structure code, and c is the soil profile permeability class.

3.4.3 Topographic Factor (LS)

The LS-factor was computed from the DEM using the LS-TOOL plugin within GISus-M (Zhang et al. 2013), following the continuous, flow-accumulation-based algorithm of Desmet and Govers (1996). This approach substitutes the standard linear slope-length term with the upslope contributing area per unit contour width, allowing the model to dynamically capture flow convergence and divergence across the catchment's complex terrain, rather than assuming uniform, unidirectional slope length. The L-factor was computed as:

$$L_{i,j} = \frac{[(A_{i,j-in} + D^2)^{m+1} - (A_{i,j-in})^{m+1}]}{[D^{m+2} * x_{i,j}^{m} * (22.13)^{m}} \quad (4)$$

where $A_{i,j\text{-}in}$ is the upslope contributing area at the inlet of grid cell (i, j) (m^2), D is the grid cell size (m), and $x_{i,j} = \sin \alpha_{i,j} + \cos \alpha_{i,j}$, with $\alpha_{i,j}$ the aspect-correction parameter for the flow direction of grid cell (i, j). The slope-length exponent m, related to the ratio of rill to inter-rill erosion (β), was computed as:

$$m = \beta / (\beta + 1) \quad (5)$$

$$\beta = (\sin \theta / 0.0896) / (3(\sin \theta)^{0.8} + 0.56) \quad (6)$$

where θ is the slope angle in degrees. Because the DEM's spatial resolution (30 m) exceeds the 4.6 m short-slope threshold below which inter-rill erosion is considered negligible (McCool et al. 1987), the model operates entirely within the valid rill-dominant erosion domain. To prevent exponential overestimation of the L-factor along high-accumulation drainage pathways, the upslope contributing area ($A_{i,j\text{-}in}$) was capped prior to calculation, using a maximum slope-length limit of 100 m a restriction consistent with the physical limits of the empirical USLE framework (Wischmeier and Smith 1978) and widely recommended for the fragmented, terraced agricultural landscapes of the Upper Blue Nile Basin (Bewket and Teferi 2009; Haregeweyn et al. 2015). The S-factor was computed following Renard et al. (1997):

$$S = \begin{cases} 10.8 \text{ x } \sin\theta + 0.03, & \text{if } \sin\theta < 0.0896 \text{ (for slopes } < 9\%) \\ 16.8 \text{ x } \sin\theta - 0.50, & \text{if } \sin\theta \geq 0.0896 \text{ (for slopes } \geq 9\%) \end{cases} \quad (7)$$

The resulting slope-length exponent m ranged continuously from approximately 0.2 to 0.5 across the catchment's slope gradients, below and above the 9% threshold (β /(β + 1)). The GIS workflow computed LS for each grid cell using this framework, producing a composite LS raster for input into the RUSLE model.

3.4.4 Support Practice Factor (P)

The P-factor accounts for the effect of soil conservation practices, such as contouring and strip cropping, in reducing soil loss relative to up-and-down-slope cultivation (Shin 1999; Lufafa et al. 2003). In the absence of region-specific mapping of conservation structures across the catchment, P-values recommended by Shin (1999) were adopted, assigned according to slope class and predominant cultivation practice. A raster P layer was generated by reclassifying the slope grid into corresponding P-values consistent with this literature-based scheme. This literature-based, slope-dependent approach was adopted due to the unavailability of field-mapped data on the spatial distribution of actual conservation structures (e.g., terraces, bunds, contour farming) across the catchment; this constraint, and its implications for model reliability, is discussed further in Section Limitations.

3.5 Cover-Management Factor (C) – Estimation Methods

The cover-management factor (C) represents the effect of vegetation, crop management, and surface cover on soil erosion by water and is a critical component of the RUSLE framework. In this study, the C-factor was estimated using three complementary approaches — literature-based (C_lit), regionally calibrated (C_reg), and remote-sensing-based (C_ndvi) to evaluate how different data sources and derivation strategies influence erosion estimates under heterogeneous land use and climatic conditions.

3.5.1 C_lit – Literature-Based C-Factor

C_lit values were assigned to land-use/land-cover (LULC) classes derived from the catchment's LULC classification (Section 3.3; overall accuracy 86.41%, Kappa = 0.8516). Due

to the fine-scale heterogeneity and limited spatial extent of individual crop parcels, the map represents cover types at an aggregated class level (e.g., cropland, seasonal residual cropland, agroforestry), comprising 12 classes in total, consistent with the classification presented in Figure 2. Field data were nonetheless collected at a finer sub-class level and assigned corresponding C_lit values based on their match to NDVI conditions, using the mean NDVI across the five representative image dates spanning the study period. C-values for each class were drawn primarily from experimental studies conducted within Ethiopian highland agro-ecosystems, principally Hurni's (1985) classification for Ethiopian highland agriculture and subsequent Ethiopia-specific regional studies; temperate-agriculture sources such as Wischmeier and Smith (1978) were used only where no regionally appropriate value existed for a given crop type, applied to a minority of classes. The full set of literature C-values considered, spanning Ethiopian highland-specific and fallback sources, is provided in Supplementary Table S1. Each LULC/crop/management class in the catchment was matched to its literature-source equivalent using three criteria: (i) agro-ecological zone correspondence (altitude band and rainfall regime), (ii) management-practice correspondence (tillage method, crop rotation, presence of conservation structures), and (iii) canopy-cover-stage correspondence (growth stage or residue-cover category). This approach assumes static surface cover within each class and does not capture temporal variation in vegetation phenology or management, potentially over- or under-estimating soil loss in areas of strong seasonal vegetation dynamics (Almagro et al. 2019).

3.5.2 C_reg – Regionally Calibrated C-Factor

The regionally calibrated C-factor (C_reg) improves on C_lit by directly integrating field observations, empirical adjustment, and local management information to capture spatial variability in soil protection more precisely than generalized literature values allow. C-factor values were assessed at 88 field plots spanning cropland, grazing land, forest, and shrubland during the 2018–2019 period, each comprising at least three reference points (approximately 285 samples in total), initially adapted from Hurni's (1985) Ethiopian USLE parameters and subsequently adjusted based on field-observed vegetation density, crop type, canopy cover, and conservation practice at each plot.

These field-adjusted values were spatially extended using a regression-based calibration framework in IBM SPSS 28.0, applying curve-estimation techniques to relate the field-assessed C-values to explanatory variables including land cover type, slope, and management intensity; satellite-derived vegetation information supported spatial interpolation but was not the primary driver, keeping the model grounded in field observations. Model performance was evaluated using R^2, RMSE, and correlation coefficient, with approximately 20% of samples (~50) held out as an independent test set for cross-validation. Adjustments explicitly accounted for the mitigating effect of conservation measures — terracing, contour ploughing, agroforestry, and vegetative buffer strips — which reduced local C-values by up to 20% relative to unprotected plots in well-managed croplands and agroforestry areas. The resulting C_reg raster shows lower values in intensively managed or densely vegetated areas and higher values in degraded cropland and heavily grazed rangeland.

3.5.3 C_ndvi – Remote-Sensing-Based C-Factor

The remote-sensing-based C-factor (C_ndvi) was derived directly from vegetation indices, providing a spatially continuous measure of vegetation cover and its erosion-protective effect. Three NDVI-based formulations were applied.

(i) Linear rescaling (Durigon et al. 2014):

$$C = (-NDVI + 1) / 2 \quad (8)$$

(ii) Exponential model (Van der Knijff et al. 2000):

$$C = \exp[-\alpha \times (NDVI / (\beta - NDVI))] \quad (9)$$

where $\alpha = 2$ and $\beta = 1$ are empirically defined curve-shaping parameters.

(iii) Precipitation-corrected crop management factor (C_PC; Felix et al. 2023; Macedo et al. 2021):

To characterize crop vulnerabilities while accounting for seasonal atmospheric constraints, Landsat 8 OLI imagery from 25 October 2019 (Path 170/Row 52) was selected. This temporal window successfully bypasses the persistent cloud cover of the peak Kiremt monsoon while capturing smallholder canopy cover near maximum greenness prior to the Bega harvest. A 25-day antecedent rainfall window (1–25 October 2019) was established to isolate immediate moisture transitions. Local gauge records indicated an accumulated rainfall (Pptx) of 36.93 mm driven entirely by early-month showers followed by ten consecutive dry days directly preceding image acquisition — compared to a 40-year (1980–2020) historical baseline mean (Lv) of 51.17 mm for the identical calendar window. Because Pptx < Lv, the catchment exhibited a distinct post-monsoon moisture deficit at the time of the satellite overpass.

To correct for moisture-induced canopy underestimation, a seasonally corrected remote-sensing framework adapted from Felix et al. (2023) was implemented. First, to compensate for water-stress-induced canopy chlorosis, the raw vegetation index (NDVI_raw) was transformed into a precipitation-corrected vegetation index (NDVI_PC) based on the localized climatic threshold:

$$NDVI_PC = \begin{cases} \text{NDVI_raw}, & \text{if Pptx} \geq \text{Lv} \\ \text{NDVI_raw} \times (\text{Lv}/\text{Pptx})^{H}, & \text{if Pptx} < \text{Lv} \end{cases} \quad (10)$$

Where H, a dimensionless moisture-sensitivity exponent was derived using the reference relationship:

$$H = (NDVI_PC - NDVI_raw) / 100 \quad (11)$$

This was computed once across catchment-representative reference clusters to isolate the magnitude of water-stress suppression. Concurrently, following Macedo et al. (2021), a scene-normalized adaptation of the Durigon rescaling equation was used to compute the baseline vegetative-cover vulnerability raster (C_r2):

$$C_r2 = (-NDVI_raw + z) / (2z) \quad (12)$$

where z is the absolute maximum NDVI value observed within the scene, scaling C_r2 strictly between 0.0 and 1.0 relative to localized vegetation boundaries. Finally, the exponent H was applied as a power term to the inverted fractional rainfall ratio and combined with the baseline raster to yield the final precipitation-corrected crop management factor:

$$C_PC = C_r2 \times (Pptx/Lv)^H \quad (13)$$

Because Pptx < Lv, the inverted rainfall ratio remains a fraction less than 1.0; raised to the power H, it produces an explicit scaling multiplier that downscales the soil-loss coefficient proportionally, preventing the final grid outputs from violating the empirical boundary constraints of the Universal Soil Loss Equation ($0 \leq C \leq 1$) and ensuring a physically consistent distribution of soil exposure across the Gilgel Abay catchment. The resulting NDVI-PC surface was validated by comparison against the corresponding raw NDVI raster for the same date (14)

3.6 Soil Loss Estimation and Sediment Delivery

Once all factor rasters (R, K, LS, C, P) were prepared, five soil-loss scenarios (A_lit, A_Durigon, A_VanderKnijff, A_PC, A_reg) were produced by substituting the respective C-factor maps into the RUSLE. Total gross erosion for the catchment under each scenario was computed by summing the pixel-based soil-loss estimates:

$$A_{total} = \sum_{i=1}^{n} (A_i \times \text{Area}_i) \quad (15)$$

where A_i is the soil loss per pixel (t ha^{-1} yr^{-1}), Area_i is the area of pixel i (ha), and n is the total number of pixels in the catchment. All RUSLE factor computation and pixel-based erosion mapping were performed in ArcGIS 10.4 using raster-based analysis at 30 m resolution.

To estimate sediment yield (SY) from soil loss, a sediment delivery ratio (SDR) approach was applied:

$$SY = SDR \times A \quad (16)$$

where SY is sediment yield (t yr^{-1}), A is mean annual soil loss (t ha^{-1} yr^{-1}), and SDR is dimensionless. To assess the sensitivity of sediment-yield estimates to SDR formulation, three independents, widely used empirical SDR models were applied to each of the five soil-loss scenarios, yielding a total of 15 SY estimates:

Williams and Berndt (1972)'s slope-based formulation:

$$SDR = 0.627 \times D^{0.403} \quad (17)$$

where D is the average percent slope of the main channel reach. Flow-path slopes were calculated using HEC-GeoHMS tools, with each grid cell along the flow path representing the outlet of its own upstream sub-catchment; the SDR raster was derived by applying equation (17) to each cell's upstream contributing slope, producing a spatially distributed SDR surface across the catchment.

Maner (1958)'s, relief–length ratio formulation:

$$\log_{10}(SDR) = 2.943 - 0.824 \times \log_{10}(R/L) \quad (18)$$

where R/L is the relief–length ratio of the catchment or sub-catchment, calculated as basin relief (maximum minus minimum elevation) divided by basin length.

Vanoni (1975)'s, basin-area formulation:

$$SDR = 0.42 \times A^{(-0.125)} \quad (19)$$

where A is basin (or sub-catchment) drainage area (mi^2), expressed in square miles as specified in the original formulation.

These three SDR models were selected to represent contrasting morphometric controls on sediment delivery — channel slope (Williams and Berndt 1972), catchment relief and drainage-path length (Maner 1958), and catchment area (Vanoni 1975) — allowing the sensitivity of sediment-yield estimates to SDR formulation to be assessed independently of the choice of C-factor scenario. This approach was adopted in preference to a connectivity-based model such as the InVEST Sediment Delivery Ratio model, which requires additional calibrated connectivity indices and deposition parameters not currently available for this catchment. Similarly, alternative distributed approaches such as the SEDD model (Ferro and Porto 2000) were not implemented here because they require spatially explicit deposition and routing parameters not currently available for this catchment.

3.6.1 Field-Based Sediment Yield Estimation

To provide an independent validation basis for the RUSLE–SDR estimates, field-based sediment yield was calculated from suspended-sediment concentration (SSC) and discharge records collected at the Bikolo (upper catchment) and Chimba (lower catchment) gauging stations over the 2012–2016 period, with daily and monthly SSC during the all seasons. Daily suspended-sediment discharge (SS) was calculated as the product of daily flow (Qw, $m^3\ s^{-1}$), daily SSC (mg L^{-1}), and the number of seconds per day, following Ladegaard-Pedersen et al. (2017).

These daily values were aggregated into a flow-weighted average SSC (C_avg) to account for the disproportionate contribution of high-flow events to total sediment transport:

$$C_{avg} = \frac{\sum_{i=1}^{n}(c_i \times t_i \times q_i)}{\sum_{i=1}^{n}(t_i \times q_i)} \quad (20)$$

where c_i is the SSC recorded at sampling time i (mg L^{-1}), q_i is the discharge at sampling time i ($m^3\ s^{-1}$), and t_i is the time interval represented by sample i (days). Field-based annual sediment yield was then computed as:

$$SY_field = Qa \times C_avg \times 31{,}536{,}000 \times 10^{-6} \quad (21)$$

where Qa is mean annual flow ($m^3\ s^{-1}$) and the constants convert the result to tonnes per year. Input parameters for both stations are summarized in Table 6 : mean annual flow was 65 $m^3\ s^{-1}$ at Bikolo (discharge range 18–320 $m^3\ s^{-1}$; SSC range 25–3,800 mg L^{-1}; C_avg = 1,814.5 mg L^{-1}) and 80 $m^3\ s^{-1}$ at Chimba (discharge range 25–250 $m^3\ s^{-1}$; SSC range 15–2,500 mg L^{-1}; C_avg = 1,068.2 mg L^{-1}). Annual sediment yield from each of the five RUSLE-based C-factor

scenarios was evaluated against this 2012–2016 field-based benchmark using percent bias (%BIAS), identifying the C-factor derivation method producing the closest agreement with observed sediment yield.

As a supplementary sensitivity check, SY_field was additionally recalculated under a series of alternative mean-annual-flow assumptions (50, 65, 75, 80, 90, and 98 $m^3 s^{-1}$, spanning the observed historical discharge range for the catchment) to illustrate how sensitive the field-based sediment-yield estimate is to the assumed representative flow value, independent of the RUSLE–SDR comparison.

3.7 Model Validation and Sensitivity Analysis

Model outputs for the five C-factor scenarios were validated through two complementary procedures. First, predicted sediment yield from each scenario was compared against observed suspended-sediment yield at the Bikolo and Chimba monitoring stations (Section 3.6.1) for 2012–2016, the most recent period for which gauge records were available, as no data were recorded for the 2019/2020 study period itself. Given the interannual variability evident in the observed record, both the five-year mean and the observed range of sediment yield were used as validation benchmarks, providing a more informative basis for assessing model plausibility than a single-value comparison. Second, percent bias (%BIAS), root-mean-square error (RMSE), Nash–Sutcliffe efficiency (NSE), and correlation coefficient (R) were computed relative to the 2012–2016 mean for each scenario. All geoprocessing and statistical analyses were performed using ArcGIS 10.4, ENVI 5.6, and IBM SPSS 28.0.

3.8 Model Assumptions and Constraints

Several design-stage constraints apply to the modelling framework used in this study. RUSLE estimates sheet and rill erosion only and does not explicitly simulate gully erosion, stream-bank erosion, channel erosion, or mass-movement processes, which may represent significant additional sediment sources in this highly dissected catchment. Because high-resolution rainfall-intensity data were unavailable, the rainfall erosivity (R) factor was estimated from an empirical relationship with mean annual precipitation (Hurni 1985) rather than from sub-daily intensity records. The support-practice (P) factor relied on literature-derived, slope-dependent values (Shin 1999) rather than field-mapped conservation structures, as detailed spatial data on terraces, bunds, and contour farming were unavailable across the catchment (Section 3.4.4). Sediment yield was estimated using three empirical sediment delivery ratio (SDR) formulations — slope-based (Williams and Berndt 1972), relief–length-ratio-based (Maner, 1958), and area-based (Vanoni 1975) — rather than a connectivity-based approach such as the InVEST Sediment Delivery Ratio model, which requires calibrated connectivity indices and deposition parameters not currently available for this catchment. Field-based sediment-yield validation (Section 3.6.1) relied on a representative mean annual flow at each gauging station rather than continuous daily discharge integration over the validation period. Model validation was based on suspended-sediment records from only two gauging stations (Bikolo and Chimba), and field-based C-factor calibration relied on 88 ground-truth plots, with a 20% subset (approximately 50 plots) used for independent cross-validation a sample density

consistent with common practice in regression-based C-factor calibration for data-scarce settings, though modest relative to the catchment's spatial extent (~1,652 km²).

4. Results

4.1 Terrain and Catchment Characteristics

The Gilgel Abay catchment, located within the Lake Tana sub-basin of the Upper Blue Nile Basin, exhibits marked topographic heterogeneity that strongly governs its hydrological and erosional dynamics. Digital Elevation Model (DEM)-derived analysis shows an elevation range of 1,788–3,534 m above sea level, reflecting a pronounced altitudinal gradient that shapes both climatic and geomorphic processes across the catchment. The mean catchment slope was computed at approximately 12.6°, indicating a dominance of moderately steep to steep terrain, particularly in the central and southern portions of the catchment. The total drainage area covers approximately 1,652 km², characterized by a well-developed dendritic drainage pattern typical of landscapes underlain by weathered volcanic formations. A computed drainage density of 1.45 km/km² indicates a highly dissected landscape with efficient surface-runoff pathways, facilitating sediment transport from upland zones toward downstream reaches. Stream-network delineation from the DEM confirmed a hierarchical flow structure, with numerous first- and second-order streams converging into the main Gilgel Abay River (Figure 1).

Terrain variability exerts a decisive influence on the spatial distribution of erosion susceptibility within the catchment. Steep mid- and lower-slope zones show the greatest potential for soil erosion, driven by the combined effects of gravitational force, concentrated flow velocity, and comparatively sparse vegetative cover, whereas the gentler-sloped, more densely vegetated upper catchment shows comparatively lower susceptibility. Together, slope steepness, elevation contrast, and drainage density illustrate the geomorphic complexity of the Gilgel Abay system, underscoring its sensitivity to land-use change and rainfall erosivity. This physiographic characterization provides the baseline terrain context against which the soil-loss and sediment-yield results presented in the following sections are interpreted.

4.2 Land Use/Land Cover Distribution

The land use/land cover (LULC) classification of the Gilgel Abay catchment (Figure 2) reveals a heterogeneous landscape dominated by agricultural activity interspersed with patches of forest, shrubland, and grassland. The classification, derived from multi-temporal Landsat imagery and validated through field observations and high-resolution Google Earth reference data, achieved an overall accuracy of 86.41% and a Kappa coefficient of 0.8516 (Table 1), indicating strong reliability of the supervised classification. Twelve LULC classes were delineated (Table 1). Cropland (annual, rain-fed) constitutes the largest proportion of the catchment, reflecting the dominance of rain-fed subsistence agriculture in the region, followed by agrofields and perennial crops, which account for a substantial share of the cultivated terrain, particularly in the mid- and lower-altitude zones. Shrubland and grassland/rangeland occupy the mid- and upper catchment zones, functioning as transitional land covers that support

grazing and broader ecosystem services. Forest plantation and dense forest occur mainly in the upper catchment and along riparian corridors, contributing to slope stabilization and runoff regulation. Bare land, bare rock, and built-up classes are distributed sporadically, concentrated on steep slopes and around settlement clusters, while water bodies (rivers, ponds, and small reservoirs) form a small but ecologically significant fraction of the landscape.

The classification results point to ongoing land-cover change consistent with growing anthropogenic pressure across the catchment. Comparison of multi-temporal Landsat imagery suggests that agricultural expansion and settlement growth have contributed to a gradual reduction in dense forest and shrubland cover, particularly in the southern and central portions of the catchment. This conversion of natural vegetation to cultivated land and bare surfaces coincides spatially with areas of elevated soil erosion susceptibility, particularly along steep agricultural slopes, while forest and grassland areas show comparatively lower erosion potential — underscoring their role in maintaining slope stability and moderating surface runoff. The high classification accuracy achieved, supported by field validation, provides confidence in the spatial reliability of the LULC dataset used for the subsequent RUSLE-based soil-erosion modelling and C-factor derivation presented in later sections.

Table 1. Accuracy assessment of LULC classification in the Gilgel Abay catchment.

Class Name	Reference Totals	Classified Totals	No. Correct	Producer's Accuracy (%)	User's Accuracy (%)
Bare rock	30	28	26	86.67	92.86
Bare land	36	45	35	97.22	77.78
Built-up	32	37	27	84.38	72.97
Stream bed	32	31	26	81.25	83.87
Cropland (annual, rain-fed)	34	33	30	88.24	90.91
Dense forest	29	28	28	96.55	100.00
Grassland/rangeland	30	33	25	83.33	75.76
Agrofields (perennial crops)	35	35	32	91.43	91.43
Forest plantation	44	42	42	95.45	100.00
Seasonal crops (irrigated/residual)	33	30	27	81.82	90.00
Shrubland	37	41	32	86.49	78.05
Water	40	29	26	65.00	89.66
Total	412	412	356	—	—
Overall Accuracy (%)					86.41%
Kappa Coefficient (κ)					0.8516

4.3 Spatial Distribution of RUSLE Factors

4.3.1 Rainfall Erosivity (R)

The rainfall–runoff erosivity (R-factor) map derived for the Gilgel Abay catchment (Figure 3a; computed following the empirical relationship and interpolation procedure described in Section

3.4.1) shows pronounced spatial variability, closely aligned with the catchment's topographic and rainfall gradients. R-factor values, expressed in $MJ \cdot mm \cdot ha^{-1} \cdot h^{-1} \cdot yr^{-1}$, ranged from 825 to 1,157, with a mean of approximately 980. The lowest erosivity values (< 900 $MJ \cdot mm \cdot ha^{-1} \cdot h^{-1} \cdot yr^{-1}$) occur predominantly in the northern and central portions of the catchment, where elevation is relatively low and rainfall intensity is moderate. Conversely, higher R-values ($> 1{,}100$ $MJ \cdot mm \cdot ha^{-1} \cdot h^{-1} \cdot yr^{-1}$) are concentrated in the southern and southeastern highland areas, corresponding to steep topographic zones that receive intense convective rainfall during the main rainy season (June–September). This spatial pattern reflects an increase in erosivity from north to south, mirroring the regional rainfall gradient and the orographic influence of the highland topography.

The observed pattern implies that the southern slopes and elevated areas of the catchment are more susceptible to rainfall-driven soil detachment and transport, particularly where land cover is sparse or cultivated fields are exposed during peak rainfall months and should be prioritized for conservation interventions such as contour bunding, terracing, and vegetative cover enhancement. These values are consistent with previously reported rainfall erosivity ranges for the Ethiopian highlands: Hurni (1985) estimated R-values between 500 and 1,500 $MJ \cdot mm \cdot ha^{-1} \cdot h^{-1} \cdot yr^{-1}$ for northwestern Ethiopia, while Panagos et al. (2023) reported national-scale erosivity estimates ranging from 400 $MJ \cdot mm \cdot ha^{-1} \cdot h^{-1} \cdot yr^{-1}$ in the arid lowlands to over 1,200 $MJ \cdot mm \cdot ha^{-1} \cdot h^{-1} \cdot yr^{-1}$ in the humid highlands. The catchment's R-values fall within this national range, supporting the regional representativeness of the derived surface. Overall, the spatially explicit R-factor distribution highlights the heterogeneity of rainfall erosivity within the catchment and its strong association with the local rainfall regime and elevation gradient, providing a basis for the subsequent soil-loss estimation and site-specific conservation planning presented in the following sections.

4.3.2 Soil Erodibility (K)

The spatial distribution of soil erodibility (K-factor) across the catchment, estimated using equation (3) and the soil texture parameters presented in Supplementary Table S2 , is shown in Figure 3b, illustrating the inherent susceptibility of soils to detachment and transport by rainfall and surface runoff. K-factor values in the study area ranged from 0.20 to 0.34 $t \cdot ha \cdot h \cdot MJ^{-1} \cdot ha^{-1} \cdot mm^{-1}$, with a mean of approximately 0.26 $t \cdot ha \cdot h \cdot MJ^{-1} \cdot ha^{-1} \cdot mm^{-1}$, indicating moderate erodibility across most of the catchment. The spatial variation of the K-factor demonstrates distinct patterns associated with soil type and topography. Higher K-values ($>$ 0.30) are concentrated in the western and northwestern parts of the catchment, where Luvisols and Nitisols dominate. These soils are typically characterized by a loamy texture, moderate organic matter content, and sub-surface clay accumulation, which increases their susceptibility to surface sealing and rill formation under intense rainfall. The northern and southwestern edge zones also show localized patches of high K-values, corresponding to areas of Leptosols, which have shallow profiles and weak structural stability.

In contrast, lower K-values (< 0.23) occur in the southern and central portions of the catchment, primarily underlain by Vertisols and well-structured Luvisols. The high clay content and swelling–shrinking behaviour of Vertisols tends to reduce soil detachability under moderate

rainfall, leading to comparatively lower erodibility. The catchment is predominantly covered by Luvisols (62.2%), followed by Nitisols (18.1%), Vertisols (9.1%), and Leptosols (6.3%), consistent with the dominant soil types described in Section 2. This composition explains the dominance of moderate-to-high K-values across the catchment: Luvisols and Nitisols, despite their relatively good fertility, are more prone to structural breakdown and crusting under intense rainfall, whereas Vertisols, though less erodible, occupy more limited, flat-lying areas, providing local resistance to erosion.

These erodibility estimates are consistent with previously reported values for the Ethiopian highlands: Hurni (1985) and Bewket and Teferi (2009) reported K-values of 0.15–0.35 $t \cdot ha \cdot h \cdot MJ^{-1} \cdot ha^{-1} \cdot mm^{-1}$ for cultivated soils in the Blue Nile basin, while Woldemariam et al. (2023) reported comparable magnitudes in adjacent catchments dominated by Luvisols and Vertisols. The current estimates thus fall within the expected range for Ethiopian uplands, supporting the validity of the soil parameterization and interpolation approach applied. Overall, the K-factor distribution reveals a moderate-to-high erodibility potential across the catchment, strongly controlled by soil type and structure; the implications of these spatial patterns for erosion risk and the prioritization of conservation interventions — particularly where high erodibility coincides with steep slopes and elevated rainfall erosivity — are examined jointly with the R-factor and soil-loss results in the Discussion.

4.3.3 Topographic Factor (LS)

The topographic (LS) factor, representing the combined influence of slope length and steepness on soil erosion potential, was derived from the DEM using the LS-TOOL module in GISus-M (Zhang et al. 2013), following equation (4). The spatial distribution of LS values across the Gilgel Abay catchment (Figure 3c) reveals substantial variability, ranging from 0.03 to 56.6, with a mean of 5.42, indicating that topography exerts a strongly heterogeneous control on erosion potential. Low LS values (< 10) dominate extensive portions of the catchment, corresponding to gently undulating uplands, floodplains, and valley bottoms where runoff energy is limited and soil detachment is minimal. Moderate values (10–15) occur on transitional mid-slope terrain, while the highest LS values (> 15) are concentrated along steep escarpments, concave slopes, valley heads, and elevated ridges areas characterized by strong slope gradients and concentrated flow accumulation, consistent with the topographic-convergence erosion mechanism described by Desmet and Govers (1996).

The marked heterogeneity of LS values reflects the catchment's rugged, dissected terrain (Section 4.1) and is broadly consistent with LS/slope–erosion relationships reported for other Ethiopian highland catchments (Hurni 1985). This indicates that LS factors derived from high-resolution DEMs provide a useful proxy for identifying zones of elevated erosion susceptibility in topographically complex watersheds such as Gilgel Abay; the spatial relationship between LS-factor patterns and the catchment's overall soil-loss distribution — including implications for the prioritization of conservation interventions in high-LS zones — is examined further, alongside the R- and K-factor results, in the Discussion.

4.3.4 Support Practice Factor (P)

The spatial distribution of the support-practice factor (P) across the Gilgel Abay catchment, derived by cross-classifying land use/land cover and slope following the Shin (1999) framework, is shown in Figure 3d. P-values ranged from 0.003 to 1 across the catchment's LULC–slope class combinations, with the lowest values (indicating more effective conservation practice) concentrated in gently sloping lowlands and valley bottoms, and the highest values (approaching 1) confined to steeply sloping upland areas with minimal conservation intervention. The southwestern and central portions of the catchment showed the lowest P-values (0.03–0.2), coinciding with agricultural zones where contour ploughing and traditional bunding are moderately implemented, consistent with the LULC–slope classification framework of Shin (1999) and Lufafa et al. (2003), whereby areas exceeding approximately 15% slope typically lack supportive practices. The mean P-factor for the catchment was estimated at approximately 0.42, indicating moderate conservation effectiveness at the catchment scale, with a substantial portion of the landscape remaining only partially protected against surface runoff and soil detachment.

4.4 C-Factor Maps and Spatial Comparison

The cover-management factor (C-factor) is a critical determinant of RUSLE model performance, representing the effectiveness of vegetation cover and land management in reducing soil exposure to erosive forces. In this study, three complementary estimation approaches were applied and compared: a literature-based approach (C_lit), a regionally calibrated field-based approach (C_reg), and a remote-sensing-based approach (C_ndvi), the latter comprising three distinct NDVI-based formulations — a linear regression (Durigon et al., 2014), an exponential regression (Van der Knijff et al., 2000), and a precipitation-corrected regression (Felix et al. 2023; Macedo et al. 2021) — yielding five spatially distinct C-factor surfaces in total. Each approach captures a different dimension of how land cover, vegetation vigour, and conservation management influence soil protection, allowing their spatial patterns and resulting soil-loss implications to be directly compared across the catchment.

4.4.1 Literature-Based C-Factor (C_lit)

The literature-based C-factor (C_lit) map was developed by assigning C-values to the catchment's 12 LULC classes following the tiered protocol described in Section 3.5.1: primarily Hurni's (1985) Ethiopian highland classification, supplemented by local Ethiopian field studies and, for a minority of classes, Wischmeier and Smith (1978), applied directly to LULC classes without seasonal or NDVI-based weighting. The resulting spatial distribution (Figure 4e) revealed pronounced contrasts across the catchment. C-values ranged from 0 to 0.4 on a pixel-wise basis, with the lowest values associated with denser, better-vegetated LULC classes and the highest values occurring over intensively cultivated, fallow, or degraded land classes. As this approach assigns a single static value per LULC class, it does not capture within-class variability in vegetation vigour, sub-crop composition, or seasonal cover dynamics — a limitation addressed by the field-calibrated and remote-sensing-based approaches presented in the following subsections.

4.4.2 Regionally Calibrated C-Factor (C_reg)

The regionally calibrated C-factor (C_reg) was derived through a field-based regression linking C-values assigned at the sub-crop/sub-practice level — compiled from Hurni (1985), local Ethiopian field studies (Hurni et al. 2015), and observed conservation practices such as terracing and agroforestry (Taye et al. 2017; Andualem and Gebremariam 2015) — to corresponding NDVI values recorded at 88 field plots (285 samples) across five observation dates spanning different phenological stages and land-cover conditions. The resulting regression equation was applied to the mean NDVI of these five time-series dates to predict C_reg across the full catchment on a pixel-wise basis. The resulting map (Figure 4f) exhibited finer spatial differentiation across land-management gradients than C_lit. C-values ranged from 0.015 to 0.49, with a mean of approximately 0.15, reflecting enhanced representation of vegetation and conservation coverage relative to C_lit. The highest C-values (> 0.25) were largely confined to degraded croplands and overgrazed grasslands, while the lowest values (< 0.1) characterized forested, terraced, and well-managed zones.

4.4.3 Remote-Sensing-Based C-Factor — Linear Model (Durigon et al. 2014)

The mean annual NDVI map (Figure 4a), was used to derive the linear NDVI-based C-factor map (Figure 4b) following the rescaling equation of Durigon, Carvalho, Antunes, Oliveira, and Fernandes (2014) (equation 8), which produced C-values ranging from 0.24 to 0.61 across the catchment. The lowest values were associated with denser vegetation cover in forested and riparian zones, while the highest values occurred over sparsely vegetated or seasonally exposed cropland, consistent with the inverse relationship between NDVI and surface protection embedded in the linear formulation. Compared with C_lit and C_reg, the Durigon-derived map provided a spatially continuous, pixel-wise representation of vegetation cover without requiring discrete LULC reclassification, capturing gradational transitions in canopy density across the catchment that the class-based approaches could not resolve.

4.4.4 Remote-Sensing-Based C-Factor — Precipitation-Corrected Model (Felix et al. 2023; Macedo et al. 2021)

The precipitation-corrected NDVI-based C-factor map (Figure 4c) derived using the moisture-correction framework of Felix et al. (2023) combined with the scene-normalized rescaling of Macedo et al. (2021) (equations 10–13), produced C-values ranging from 0.21 to 0.52 across the catchment. This method incorporated the antecedent moisture deficit observed ahead of the 25 October 2019 image acquisition (Pptx = 36.93 mm, below the 40-year calendar-window mean of 51.17 mm; Section 3.5.3), adjusting the baseline vegetative-cover raster to account for the reduced canopy greenness associated with this post-Kiremt dry transition. The lowest C-values were associated with denser, less moisture-stressed vegetation, while the highest values occurred in areas where seasonal drying had suppressed apparent canopy cover, distinguishing this method from the uncorrected NDVI-based approaches by explicitly incorporating short-term rainfall variability into the C-factor estimate.

4.4.5 Remote-Sensing-Based C-Factor — Exponential Model (Van der Knijff et al. 2000)

The exponential NDVI-based C-factor map (Figure 4d) derived following Van der Knijff et al. (2000) (equation 9), produced raw pixel values ranging from 0.21 to 1.91. Values exceeding

the physically valid upper bound of the RUSLE C-factor (C = 1) occurred over a small number of pixels with negative NDVI, corresponding to open-water surfaces and exposed rock — a known mathematical property of the exponential formulation as NDVI approaches the β parameter. All pixel values ≥ 1 were capped at C = 1 prior to use in RUSLE computation, consistent with the physical bounds of the RUSLE framework; this capping was not separately visualized in Figure 4d, which displays the resulting capped surface. Within the valid range, the lowest C-values corresponded to densely vegetated forest and riparian zones, while the highest values occurred over sparsely vegetated and bare cropland areas, showing the sharper, non-linear response of this exponential formulation to changes in NDVI relative to the linear (Durigon et al. 2014) and precipitation-corrected (Felix et al. 2023 and Macedo et al. 2021) approaches.

4.4.6 Validation of C-Factor Methods Against Field-Observed Values

Predicted C-values from each of the five derivation methods were compared against field-observed C-values at the validation subset of ground-truth plots (Section 3.7), using the coefficient of determination (R^2) and root-mean-square error (RMSE) as performance metrics (Figure 5). The field-calibrated regression method (C_reg) showed the strongest agreement with observed values (R^2 = 0.923, RMSE = 0.013), consistent with its direct derivation from field-based C-value observations. Among the NDVI-based approaches, the Durigon et al. (2014) linear model (R^2 = 0.872, RMSE = 0.220) and the Van der Knijff et al. (2000) exponential model (R^2 = 0.801, RMSE = 0.320) showed comparatively strong correlation with observed values, though with higher error magnitude than C_reg. The precipitation-corrected model (Felix et al., 2023; Macedo et al., 2021) showed moderate agreement (R^2 = 0.572, RMSE = 0.132). The literature-based method (C_lit) showed the weakest correlation with field-observed values (R^2 = 0.308, RMSE = 0.140), reflecting its reliance on static, class-level values rather than plot-specific field conditions. The underlying regression relating field-observed C-values to NDVI, used to calibrate the empirical (C_reg) model, is shown in Figure 6 ($C = 8.9075e^{-14.44} \times NDVI$, R^2 = 0.729). Validation of C-factor methods against field-observed values shown in Table 2.

Table 2. Validation of C-factor methods against field-observed values.

Method	R^2	RMSE
Durigon (2014)	0.872	0.220
Felix & Macedo (2023/2021)	0.572	0.132
Van der Knijff (2000)	0.802	0.320
Literature-based (C_lit)	0.308	0.140
Empirical regression (C_reg)	0.923	0.013

4.5 Soil Loss Estimation under Different C-Factor Scenarios

4.5.1 Spatial Patterns

The spatial distribution of soil loss was estimated under all five C-factor derivation methods examined in this study — the linear NDVI regression of Durigon et al. (2014), the exponential NDVI regression of Van der Knijff et al. (2000), the precipitation-corrected NDVI approach of Felix et al. (2023) and Macedo et al. (2021), the literature-based scenario (A_lit), and the locally field-calibrated regression scenario (A_reg). The spatial distributions generated by the five scenarios are presented in Figure 7a–e. These spatial patterns are strongly governed by the interplay between topography, land use, and vegetation cover conditions, which have been previously emphasized as key erosion drivers in the Upper Blue Nile Basin (Balabathina et al. 2020; Gashaw et al. 2020). Across all five scenarios, soil erosion hotspots were concentrated in the steep upland areas of the northwestern and central sub-catchments, where slopes exceed 20% and croplands and grazing lands dominate. In contrast, the relatively flat valley floors and well-vegetated areas along river corridors exhibited minimal soil loss, consistent with findings from similar topographic catchments in Ethiopia (Zerihun et al. 2018; Tsegaye and Bharti 2021).

Quantitatively, mean annual soil loss differed markedly among the five methods (Table 3). The exponential NDVI regression (Van der Knijff et al. 2000) produced the highest estimates (0.01–478.41 t ha^{-1} yr^{-1}, mean = 99.88 t ha^{-1} yr^{-1}, SD = 22.73), corresponding to a total catchment soil loss of approximately 37.79 million t yr^{-1}. The linear NDVI regression (Durigon et al., 2014) produced the second-highest estimates (0.01–243.73 t ha^{-1} yr^{-1}, mean = 78.86 t ha^{-1} yr^{-1}, SD = 16.07; total ≈ 29.84 million t yr^{-1}), followed by the precipitation-corrected NDVI approach (Felix et al., 2023; Macedo et al., 2021), which yielded intermediate values (0.00–118.25 t ha^{-1} yr^{-1}, mean = 57.89 t ha^{-1} yr^{-1}, SD = 10.61; total ≈ 21.90 million t yr^{-1}). The literature-based scenario (A_lit) produced markedly lower estimates (0.00–196.64 t ha^{-1} yr^{-1}, mean = 43.19 t ha^{-1} yr^{-1}, SD = 10.86; total ≈ 16.34 million t yr^{-1}), reflecting its reliance on static, class-averaged C-values that do not capture within-class vegetation variability. The locally field-calibrated regression scenario (A_reg) produced the lowest and least variable estimates of all five methods (0.00–88.20 t ha^{-1} yr^{-1}, mean = 31.47 t ha^{-1} yr^{-1}, SD = 6.15; total ≈ 11.91 million t yr^{-1}), consistent with its grounding in field-observed management and conservation-practice adjustments (Section 3.5.2) that moderate erosion estimates relative to the uncorrected NDVI-based approaches.

The pronounced divergence among the three NDVI-based methods themselves — despite all three deriving C from the same underlying vegetation index — illustrates that the choice of regression form (linear, exponential, or precipitation-corrected) is itself a major source of uncertainty in RUSLE-based soil-loss estimation, independent of the broader literature-vs-remote-sensing distinction emphasized in prior regional studies (Mahgoub et al. 2024).

Table 3. Summary statistics of mean annual soil loss (A, t ha^{-1} yr^{-1}) under five C-factor derivation methods

C-factor method	Area (ha)	Min	Max	Mean	SD	Total (t yr^{-1})
Van der Knijff et al. (2000)	378,330	0.01	478.41	99.88	22.73	37,788,064

Durigon et al. (2014)	378,330	0.01	243.73	78.86	16.07	29,836,338
Felix (2023) / Macedo (2021)	378,330	0.00	118.25	57.89	10.61	21,900,134
Literature-based (A_lit)	378,330	0.00	196.64	43.19	10.86	16,341,567
Field-calibrated regression (A_reg)	378,330	0.00	88.20	31.47	6.15	11,893,945

The field-calibrated regression scenario (A_reg) showed the following distribution of soil-loss severity across the catchment (Table 4):

Table 4. Distribution of soil-loss severity classes under the field-calibrated regression (A_reg) C-factor scenario.

Severity class (t ha^{-1} yr^{-1})	Area (ha)	Mean (t ha^{-1} yr^{-1})	SD	Total soil loss (t yr^{-1})	Contribution (%)
0–1	11,158	0.77	6.50	8,556	0.07
1–5	77,374	3.47	2.40	268,857	2.26
5–10	84,234	7.35	3.62	619,249	5.21
10–20	73,714	14.55	7.25	1,072,721	9.02
20–50	63,156	32.45	14.45	2,049,118	17.23
>50	68,629	114.75	42.37	7,875,444	66.21
Total	378,330	—	—	11,893,945	100%

This severity-class breakdown reveals a strongly disproportionate erosion pattern: land falling within the highest severity category (> 50 t ha^{-1} yr^{-1}) occupies only about 18% of the catchment's total area (68,629 of 378,330 ha) yet contributes 66.21% of total annual soil loss, while the lowest severity classes (0–5 t ha^{-1} yr^{-1}), covering roughly 23% of the catchment, contribute less than 2.3% of total soil loss combined. This concentration of erosion within a relatively small, high-severity land area is consistent with slope- and cover-driven erosion hotspot patterns reported elsewhere in the Ethiopian highlands (Zerihun et al. 2018) and directly informs the spatial targeting of conservation interventions discussed in Section Discussion.

4.6 Spatial Distribution of the Sediment Delivery Ratio

Figure 8 (a-b). Spatial distribution of the Sediment Delivery Ratio (SDR) across the Gilgel Abay catchment: (a) sub-catchment-level SDR derived using the Maner (1958) relief–length ratio formulation, ranging from 0.19 to 0.23; and (b) pixel-level SDR derived using the Williams and Berndt (1972) slope-based formulation, ranging from 0.0187 to 0.1617.

The spatial distribution of the sediment delivery ratio (SDR) across the Gilgel Abay catchment was derived using two complementary formulations. At the pixel level, SDR was computed using the Williams and Berndt (1972) slope-based formulation (equation 17), with average

channel-reach slope derived from DEM-based flow accumulation at each pixel; resulting values ranged from 0.0187 to 0.1617 along the stream network (Figure 8b), with the highest values concentrated toward the lower reaches near the catchment outlet, reflecting locally steeper channel gradients. At the sub-catchment scale, SDR was computed using the relief–length ratio formulation of Maner (1958) (equation 18), with basin relief (headwater-to-outlet elevation difference) and basin length measured for each of the catchment's 13 delineated sub-catchments; resulting values ranged from 0.19 to 0.23 (Figure 8a). Sub-catchment 1, at the catchment outlet, showed the highest SDR (0.23), while sub-catchment 8, along the western catchment margin, showed the lowest (0.19).

4.6.1 Sediment Yield Estimates under Alternative C-Factor Scenarios

Sediment yield (SY) was estimated for each of the five C-factor scenarios by applying three catchment-scale SDR values to the corresponding total gross erosion (A) for each scenario (Table 5): the area-weighted mean of the pixel-level Williams and Berndt (1972) SDR raster (SDR = 0.110), the mean of the sub-catchment-scale Maner (1958) SDR values (SDR = 0.203), and the Vanoni (1975) area-based SDR computed from the total catchment area of 1,652 km² (638.0 mi²; SDR = 0.187). Resulting sediment-yield estimates ranged from 1.31 to 4.15 million t yr^{-1} (Williams and Berndt 1972), 2.41 to 7.67 million t yr^{-1} (Maner 1958), and 2.22 to 7.07 million t yr^{-1} (Vanoni 1975). Across all three formulations, the Van der Knijff et al. (2000) scenario consistently produced the highest sediment yield, while the field-calibrated regression scenario consistently produced the lowest.

Table 5. Sediment yield estimates for the Gilgel Abay catchment under five C-factor scenarios and three SDR formulations.

Model	A (t yr^{-1})	SY — Williams & Berndt, slope-based (SDR = 0.110)	SY — Maner, relief/length-based (SDR = 0.203)	SY — Vanoni, area-based (SDR = 0.187)
Van der Knijff (2000)	37,788,064	4,150,076	7,670,952	7,067,369
Durigon (2014)	29,836,338	3,276,663	6,055,758	5,580,594
Felix (2023)/Macedo (2021)	21,900,134	2,405,283	4,445,714	4,097,915
Local (Lit)	16,341,567	1,794,713	3,317,326	3,057,762
Empirical regression	11,893,945	1,306,167	2,414,459	2,224,635

4.6.2 Relationships between SDR and Morphometric Parameters

The relationships between SDR and selected morphometric parameters are presented in Figures 9(a-b) and 10. SDR exhibited a positive nonlinear relationship with slope percentage (Figure 9a). In contrast, SDR showed an inverse relationship with the L/R ratio, where L represents flow-path length and R represents the radius of curvature (Figure 9b). SDR also exhibited an inverse relationship with basin area (Figure 10), consistent with the Vanoni (1975) area-based

SDR formulation applied at the catchment scale (Section 4.6.1). Smaller sub-catchments generally showed higher SDR values, whereas larger sub-catchments showed lower SDR values, with sub-catchment SDR values ranging narrowly between approximately 0.19 and 0.24 across basin areas of 100–500 km².

4.6.3 Validation of Sediment-Yield Estimates

Field-based sediment yield, calculated using equations (20)–(21) from the Bikolo and Chimba gauge records (Section 3.6.1), is summarized in Table 6. The two-station average (3,207,000 t yr^{-1}) was used as the validation benchmark for the model-based estimates.

Table 6. Field-based sediment yield estimates (SY_field) for the Bikolo and Chimba gauging stations, 2012–2016.

Station	Qa ($m^3 s^{-1}$)	C_avg (mg L^{-1})	SY_field (t yr^{-1})
Bikolo (upper)	65	1,814.5	3,719,000
Chimba (lower)	80	1,068.2	2,695,000
Average (validation benchmark)	—	—	3,207,000

Model-based sediment-yield estimates for the five C-factor scenarios (Table 5) were validated against this benchmark using percent bias (%BIAS) across all three SDR formulations (Table 7).

Table 7. Percent bias (%BIAS) of modelled sediment yield relative to the observed field-based benchmark (3,207,000 t yr^{-1}), for five C-factor scenarios under three SDR formulations.

Model	SY — Williams & Berndt (t yr^{-1})	%BIAS	SY — Maner (t yr^{-1})	%BIAS	SY — Vanoni (t yr^{-1})	%BIAS
Van der Knijff (2000)	4,150,076	+29.4%	7,670,952	+139.2%	7,067,369	+120.4%
Durigon (2014)	3,276,663	+2.2%	6,055,758	+88.8%	5,580,594	+74.0%
Felix (2023)/Macedo (2021)	2,405,283	−25.0%	4,445,714	+38.6%	4,097,915	+27.8%
Local (Hurni,1985)	1,794,713	−44.0%	3,317,326	+3.4%	3,057,762	−4.7%
Empirical regression	1,306,167	−59.3%	2,414,459	−24.7%	2,224,635	−30.6%

Agreement varied substantially depending on both the C-factor method and the SDR formulation applied. Under the Williams and Berndt (1972) SDR, the Durigon et al. (2014) scenario showed the closest agreement with observed sediment yield (%BIAS = +2.2%). Under the Maner (1958) and Vanoni (1975) SDR formulations, the literature-based (Hurni 1985)

scenario showed the closest agreement (%BIAS = +3.4% and −4.7%, respectively). The Van der Knijff et al. (2000) scenario consistently produced the largest positive bias across all three SDR formulations (+29.4% to +139.2%), while the empirical regression scenario consistently underestimated observed sediment yield (%BIAS = −24.7% to −59.3%).

4.6.4 Validation Assessment and Uncertainty

Across the 15 model ×SDR combinations (five C-factor scenarios × three SDR formulations), sediment-yield estimates ranged from 1,306,167 to 7,670,952 t yr^{-1}, with a mean of 4,257,692 t yr^{-1}, a standard deviation of approximately 1,890,000 t yr^{-1}, and a coefficient of variation of approximately 44%, reflecting substantial combined sensitivity to both C-factor derivation method and SDR formulation. No single C-factor scenario showed consistently close agreement with the observed benchmark across all three SDR formulations (Table 6): the Durigon et al. (2014) scenario performed best under the Williams and Berndt (1972) SDR, while the literature-based (Hurni 1985) scenario performed best under both the Maner (1958) and Vanoni (1975) SDR formulations. This indicates that model uncertainty in this study arises jointly from C-factor parameterization and SDR formulation, rather than from either source alone, and that validation performance should be interpreted with respect to the specific SDR method applied rather than treated as a single, method-independent ranking of C-factor approaches.

These findings should also be interpreted in light of the substantial difference between gross hillslope erosion (A) and sediment yield at the catchment outlet: the Williams and Berndt (1972) SDR (mean ≈ 0.11) indicates that only approximately 11% of gross erosion is delivered to the outlet under this formulation, with the remaining material deposited or stored within hillslopes, valley bottoms, and channel reaches before reaching the monitoring stations. This is consistent with the pronounced spatial concentration of soil loss identified in the severity-class analysis (Table 4), where a relatively small proportion of the catchment — predominantly steep, degraded, or intensively cultivated upland slopes — accounts for the large majority of total gross erosion, while much of this material is likely trapped locally rather than transported to the outlet. Among the five C-factor scenarios, the field-calibrated empirical regression produced the most internally consistent behaviour across both the C-factor validation (Section 4.4.6, R^2 = 0.923) and the sediment-yield comparison, consistently yielding the most conservative soil-loss and sediment-yield estimates; while it did not always show the closest numerical agreement with the observed benchmark, its coherence across independent validation steps supports its plausibility as a physically grounded, locally calibrated estimate for this catchment.

5. Discussion

This study evaluated how five alternative C-factor derivation methods — a literature-based scenario (A_lit), a locally field-calibrated regression (A_reg), and three NDVI-based formulations (Durigon et al. 2014; Van der Knijff et al. 2000; Felix et al. 2023; Macedo et al. 2021) — influence RUSLE-based soil-loss and sediment-yield predictions in the Gilgel Abay

catchment, and validated the resulting estimates against independently observed field data and three sediment-delivery-ratio (SDR) formulations. The results demonstrate that C-factor selection is a first-order source of variability in both soil-loss magnitude and sediment-yield agreement with observations — a finding consistent with, and adding empirical weight to, prior assessments identifying the C-factor as the dominant source of uncertainty in RUSLE applications (Guzha et al. 2018; Panagos et al. 2023).

5.1 Influence of C-Factor Parameterization on Soil Loss

Total estimated annual gross soil loss varied more than threefold across the five scenarios, from 11.89 million t yr^{-1} under the field-calibrated regression (A_reg) to 37.79 million t yr^{-1} under the Van der Knijff et al. (2000) exponential formulation (Table 3). This range is not a modelling artefact but a direct consequence of how differently each method translates vegetation information into a cover-protection value: the exponential and linear NDVI formulations (Van der Knijff et al. 2000; Durigon et al 2014) respond steeply to small differences in NDVI at low-to-moderate vegetation cover, amplifying the effect of sparse or seasonally exposed vegetation, whereas the field-calibrated regression is anchored directly to observed conservation practices and management conditions at 88 ground-truth plots, tending to produce more conservative estimates. This pattern — that mathematically distinct formulations applied to the same underlying NDVI signal can diverge substantially — reinforces a central methodological point raised in the Introduction: the choice of NDVI-to-C transfer function matters independently of the choice of vegetation index itself. The consistency of this ranking across the severity-class analysis (Table 4), where the highest-erosion class (>50 t ha^{-1} yr^{-1}) occupied only 18.14% of the catchment yet contributed 66.21% of total classified soil loss under A_reg, further indicates that erosion in this catchment is spatially concentrated on a relatively small proportion of steep, degraded, or intensively cultivated slopes rather than distributed evenly — a pattern with direct implications for targeted, rather than catchment-wide, conservation planning (Section 5.4).

5.2 Sediment Delivery Ratio and the Gap between Gross Erosion and Sediment Yield

The substantial difference between gross hillslope erosion (A) and sediment yield at the catchment outlet is one of the more informative findings of this study. Under the spatially distributed Williams and Berndt (1972) SDR (mean ≈ 0.11), only approximately 11% of gross erosion was estimated to reach the catchment outlet, with the remainder deposited or stored within hillslopes, valley bottoms, and channel reaches before reaching the monitoring stations. This finding is consistent with established SDR theory, in which delivery ratios well below unity are expected in larger, topographically complex catchments (Walling, 1983; de Vente et al., 2008), and it explains why gross soil-loss totals in this study (11.9–37.8 million t yr^{-1}) are an order of magnitude larger than corresponding sediment-yield estimates (1.3–7.7 million t yr^{-1}; Table 6). The inverse relationship observed between SDR and basin area (Figure 10), and the positive relationship between SDR and channel slope (Figure 9a), are consistent with the conceptual basis of all three SDR formulations applied here (Williams and Berndt, 1972; Maner 1958; Vanoni 1975), though these relationships should be interpreted as empirical associations rather than direct evidence of the underlying transport mechanisms, since slope, drainage density, land cover, and soil properties covary across the catchment's sub-basins and

a static SDR does not capture event-scale variability in runoff, antecedent moisture, or channel remobilization.

5.3 Validation Performance and Method Uncertainty

No single C-factor scenario showed consistently close agreement with the observed sediment-yield benchmark (3,207,000 t yr^{-1}, derived from the Bikolo and Chimba gauge records) across all three SDR formulations (Table 6). The Durigon et al. (2014) linear NDVI scenario showed the closest agreement under the Williams and Berndt (1972) SDR (%BIAS = +2.2%), while the literature-based (Hurni 1985) scenario showed the closest agreement under both the Maner (1958) and Vanoni (1975) formulations (%BIAS = +3.4% and −4.7%, respectively). This result is itself informative: it demonstrates that sediment-yield validation outcomes in this catchment are jointly determined by C-factor parameterization and SDR formulation, and that neither can be evaluated independently of the other. A ranking of "best" C-factor method is therefore inherently conditional on the SDR approach used alongside it, a nuance not always made explicit in single-SDR RUSLE studies in the region (Balabathina et al. 2020; Mengie et al. 2019; Tsegaye and Bharti 2021). The Van der Knijff et al. (2000) scenario consistently produced the largest positive bias across all SDR formulations (+29.4% to +139.2%), indicating a persistent tendency toward overestimation traceable to the steep, non-linear response of its exponential formulation, including the small number of pixels requiring capping at the RUSLE-valid upper bound (C = 1; Section 4.4.5). Conversely, while the field-calibrated empirical regression did not consistently produce the closest numerical match to the observed benchmark, it showed the strongest and most internally consistent validation performance against field-observed C-values directly (R^2 = 0.923; Section 4.4.6), the lowest and most conservative soil-loss and sediment-yield estimates throughout, and coherent behaviour across every independent check applied in this study. This combination of qualities — even without claiming the closest single-point match to the sediment-yield benchmark — supports its interpretation as the most physically grounded and locally defensible C-factor estimate for this catchment, consistent with the broader argument, developed in the Introduction, that field-informed, regionally calibrated parameterization is preferable to the uncritical transfer of generalized coefficients.

5.4 Implications for Soil and Water Conservation Prioritization

The concentration of soil loss within a relatively small area of the catchment — steep, degraded, or intensively cultivated slopes, primarily in the northwestern and central sub-catchments — combined with the spatial pattern of SDR (highest in the southern and southeastern sub-catchments, and in smaller, steeper sub-catchments generally) provides a more targeted basis for conservation prioritization than average catchment-wide soil-loss statistics alone. Areas combining high modelled soil loss with high SDR are the most likely to contribute sediment to the stream network and, ultimately, to Lake Tana's siltation, and are therefore reasonable priority candidates for interventions such as contour bunds, terracing, vegetative buffer strips, and agroforestry (Taye et al. 2017; Belayneh et al. 2019). However, the appropriate choice and design of such interventions should be guided by field verification of slope, soil depth, land tenure, and current farming practice, rather than applied uniformly

based on modelled outputs alone, consistent with evidence from Ethiopian highland studies that the effectiveness of conservation structures can change over time as they accumulate sediment and storage capacity declines.

5.5 Comparison with Independently Published Estimates

The long-term NDVI examination to place the 2019/2020 study period within a longer-term vegetation context, mean NDVI was examined over 2001–2020 using Google Earth Engine-derived Landsat archive imagery, independent of the core five-method C-factor comparison (Supplementary Figures S1). The primary field-based sediment-yield benchmark derived in this study (approximately 3.2 million t yr^{-1}) sits within, though toward the upper end of, the range reported by other modelling approaches applied to the Gilgel Abay catchment, which have reported sediment-yield estimates spanning roughly 0.4 to 5.1 million t yr^{-1} depending on model structure (process-based SWAT applications, scenario-based land-management modelling, and machine-learning approaches). This range of published estimates spanning more than an order of magnitude across different modelling frameworks underscores that the uncertainty identified within this study's five-C-factor, three-SDR comparison is not unique to this analysis, but reflects a broader, structural uncertainty in sediment-yield estimation for this catchment that is only partially attributable to C-factor choice (Table 8).

Table 8. Comparison of model-based and field-based sediment yield estimates with previously published studies for the Gilgel Abay catchment.

Source	Method	SY (t yr^{-1})	Comparison with this study
Alebachew, Wolka, Molla, Emiru, Dengiz, & Agbor (2025), Scientific Reports	SWAT process-based model	61,575–318,233 (mean 184,695)	Substantially lower than this study's full range
Belay (2019), M.Sc. thesis, IIT Roorkee	SWAT scenario modelling	388,000	Lower than this study's range
Worku, Zimale, Francke, Zargar, & Bronstert (2026)	Machine-learning sedigraph reconstruction	4,500,000–5,100,000	Higher than this study's range — plausibly closer to gross erosion than delivered sediment yield
This study (model-based, five C-factor scenarios × three SDR formulations)	RUSLE–SDR	1,306,167–7,670,952	Spans the full range of published estimates
This study (field-based, Bikolo/Chimba average, 2012–2016)	Direct gauge measurement	3,207,000	Falls within the upper portion of the machine-learning range, well above the SWAT-based estimates

5.6 Limitations

Several limitations should be considered when interpreting these results. RUSLE estimates sheet and rill erosion only and does not explicitly represent gully erosion, stream-bank erosion,

channel erosion, or mass-movement processes, which may be significant additional sediment sources in this highly dissected catchment. The rainfall erosivity (R) factor was derived from an empirical relationship with mean annual precipitation (Hurni 1985) rather than from sub-daily rainfall-intensity records, which may not fully capture the erosive effect of individual extreme events. The support-practice (P) factor relied on literature-derived, slope-dependent values (Shin 1999) rather than field-mapped conservation structures, since detailed spatial data on terraces, bunds, and contour farming were unavailable across the catchment. Remote-sensing-derived C-factors are subject to further uncertainty from atmospheric correction, soil-background effects, and seasonal phenology; a supplementary comparison between SAVI and the NDVI-based output for this study revealed pronounced deviation over open-water surfaces and specific vegetation classes, indicating that SAVI's fixed soil-brightness correction was not well suited to this catchment's mixed land-cover conditions, and NDVI was therefore retained as the primary basis for C-factor derivation, tested through multiple complementary formulations rather than substituted for an index offering no demonstrated advantage here.

Sediment-yield validation relied on suspended-sediment records from only two gauging stations (Bikolo and Chimba) covering 2012–2016, as no gauge data were available for the 2019/2020 study period itself; any land-use change between these two periods represents an additional, unquantified source of uncertainty, and validation at only two stations limits assessment of model performance across the full spatial extent of the catchment. The SDR approach applied here, while tested through three independent formulations, remains a static, empirically derived ratio that does not capture event-scale changes in sediment connectivity, channel storage, or floodplain deposition; comparison with dynamic sediment-routing models (e.g., SWAT) or connectivity-index-based SDR approaches would strengthen future assessments. Finally, field-based C-factor calibration relied on 88 ground-truth plots (approximately 285 individual sample points), with a 20% subset used for independent cross-validation; while consistent with common practice for field-informed calibration in data-scarce settings, this sample density is modest relative to the catchment's spatial extent, and denser or more quantitative field sampling would further strengthen confidence in the calibration.

5.7 Overall Implication

Taken together, these findings show that C-factor selection substantially affects both soil-loss magnitude and sediment-yield prediction in the Gilgel Abay catchment, and that this effect cannot be evaluated independently of the SDR formulation used to convert gross erosion into sediment yield. The study's main contribution is therefore not to identify a single universally superior C-factor method, but to demonstrate, empirically, that vegetation parameterization must be evaluated against local field observations and interpreted jointly with sediment-delivery assumptions, rather than adopted by convention. The field-calibrated, locally informed approach developed in this study offers a transferable protocol for other data-scarce Ethiopian highland catchments facing similar constraints, while the NDVI-based formulations, despite their higher sensitivity to overestimation in this analysis, remain valuable for their spatial continuity and potential for monitoring vegetation change over time, provided their outputs are cross-checked against field or gauge observations before being applied unconditionally elsewhere.

6. Conclusions and Recommendations

6.1 Conclusions

This study evaluated the influence of five alternative C-factor estimation methods — a literature-based scenario (A_lit), a locally field-calibrated regression scenario (A_reg), and three NDVI-based formulations (Durigon et al., 2014; Van der Knijff et al., 2000; Felix et al., 2023/Macedo et al., 2021) — on soil-loss and sediment-yield predictions in the Gilgel Abay catchment of the Lake Tana sub-basin, northwestern Ethiopia, and validated the resulting estimates against independently observed field data using three sediment-delivery-ratio (SDR) formulations (Williams and Berndt 1972; Maner 1958; Vanoni 1975). To our knowledge, this is the first study in this catchment to compare multiple C-factor derivation methods within a single RUSLE framework and evaluate each against field-based sediment-yield observations across multiple SDR formulations, directly addressing a gap in prior regional RUSLE applications, which have generally relied on a single C-factor method without such benchmarking.

The results demonstrate that C-factor selection is a first-order source of uncertainty in RUSLE-based erosion assessment. Total estimated annual gross soil loss ranged more than threefold across the five scenarios, from 11.89 million t yr^{-1} under the field-calibrated regression to 37.79 million t yr^{-1} under the Van der Knijff et al. (2000) exponential formulation. Soil loss was spatially concentrated: under the field-calibrated regression scenario, areas exceeding 50 t ha^{-1} yr^{-1} occupied only 18.14% of the catchment yet contributed 66.21% of total classified soil loss, identifying a relatively limited area as the dominant source of modelled erosion.

Sediment-delivery-ratio analysis indicated that only a fraction of gross hillslope erosion reaches the catchment outlet: the spatially distributed Williams and Berndt (1972) SDR (mean ≈ 0.11) indicates that approximately 11% of gross erosion is delivered downstream, with the remainder deposited or stored within the catchment. SDR values showed a positive relationship with channel slope and an inverse relationship with basin area and the L/R ratio, consistent with established sediment-delivery theory. Across the fifteen model × SDR combinations evaluated, sediment-yield estimates ranged from 1.31 to 7.67 million t yr^{-1}, against a field-based observed benchmark of approximately 3.21 million t yr^{-1} derived from the Bikolo and Chimba gauging stations (2012–2016). No single C-factor method showed consistently close agreement with this benchmark across all three SDR formulations: the Durigon et al. (2014) formulation performed best under the Williams and Berndt (1972) SDR (%BIAS = +2.2%), while the literature-based (Hurni 1985) scenario performed best under the Maner (1958) and Vanoni (1975) formulations (%BIAS = +3.4% and −4.7%, respectively). The Van der Knijff et al. (2000) formulation consistently overestimated sediment yield across all SDR formulations, while the field-calibrated regression, despite not always matching the benchmark most closely in absolute terms, showed the strongest and most internally consistent validation performance against field-observed C-values (R^2 = 0.923) and the most conservative, physically coherent estimates throughout.

Overall, the findings indicate that no single C-factor derivation method is universally superior; rather, model reliability depends jointly on the C-factor parameterization and the SDR

formulation applied. Locally field-calibrated approaches, grounded in observed vegetation and management conditions, provide the most internally consistent and defensible basis for erosion assessment in this data-scarce highland catchment, while NDVI-based formulations, particularly those with strongly non-linear response functions, require careful validation before being applied without field cross-checking.

6.2 Recommendations

The findings support a targeted and locally adapted soil and water conservation strategy for the Gilgel Abay catchment. Priority should be given to steep, degraded, and intensively cultivated areas with estimated soil losses exceeding 50 t ha^{-1} yr^{-1}, particularly where these areas overlap with sub-catchments having high sediment-delivery potential. This approach can improve the allocation of conservation resources by focusing interventions on areas likely to contribute substantially to catchment-scale sediment loss.

Conservation measures should be selected through field verification and participatory planning. Depending on local biophysical and socioeconomic conditions, appropriate interventions may include contour bunds, terraces, vegetative buffer strips, agroforestry, conservation tillage, cover crops, and gully-control structures. These measures should not be prescribed solely from modelled outputs; local knowledge, land-tenure conditions, farmer priorities, and maintenance requirements should also inform their design and implementation.

The sensitivity of model performance to the C-factor and SDR formulation highlights the need for locally validated methods. Field-calibrated C-factor relationships should be preferred where sufficient observations are available, whereas NDVI-based estimates should be cross-validated against field or gauge observations before operational application. Future studies should compare alternative SDR formulations and assess dynamic or connectivity-based sediment-routing approaches alongside static empirical methods.

Validation should be strengthened by expanding monitoring at the Bikolo and Chimba stations and, where feasible, at intermediate locations. Event-based measurements of rainfall, runoff, and suspended sediment, together with validation periods independent of model calibration, would reduce temporal mismatch and improve assessment of model transferability. Multi-date and multi-sensor imagery, including Sentinel-2, Landsat, and MODIS, should also be evaluated to better represent seasonal vegetation dynamics and reduce uncertainty related to cloud cover, soil-background reflectance, and NDVI saturation.

Overall, remote sensing and modelling should guide the spatial prioritization of conservation activities, while final intervention choices should be confirmed through field assessment and community engagement. This integrated approach provides a more defensible basis for reducing soil erosion and sediment delivery in the Gilgel Abay catchment and comparable Ethiopian highland environments.

References

Alebachew ED, Wolka K, Molla MB, Emiru NC, Dengiz O, Agbor DT (2025) SWAT-based soil erosion and sediment yield modeling in the upper Gilgel Abay catchment, Blue Nile Basin, Ethiopia. Sci Rep 15:28821. https://doi.org/10.1038/s41598-025-09367-3

Almagro A, Thomé TC, Colman CB, Pereira RB, Marcato Junior J, Rodrigues DBB, Oliveira PTS (2019) Improving cover and management factor (C-factor) estimation using remote sensing approaches for tropical regions. Int Soil Water Conserv Res 7(4):325–334. https://doi.org/10.1016/j.iswcr.2019.08.005

AL-Somaydaii JA, Abdaljader A (2024) Modeling of spatially distributed sedimentation in Houran dam H-3. AIP Conf Proc 3009(1):030125. https://doi.org/10.1063/5.0190480

Andualem TG, Gebremariam B (2015) Impact of land use land cover change on streamflow and sediment yield: a case study of Gilgel Abay watershed, Lake Tana sub-basin, Ethiopia. Int J Technol Enhanc Emerg Eng Res 3(11):28–42

Assaf AT, Sayl KN, Adham A (2021) Surface water detection method for water resources management. J Phys Conf Ser 1973:012149. https://doi.org/10.1088/1742-6596/1973/1/012149

Balabathina VN, Raju RP, Mulualem W, Tadele G (2020) Estimation of soil loss using remote sensing and GIS-based universal soil loss equation in northern catchment of Lake Tana sub-basin, Upper Blue Nile Basin, Northwest Ethiopia. Environ Syst Res 9:16. https://doi.org/10.1186/s40068-020-00203-3

Belay AD (2019) Hydrological modeling of Gilgel Abay river basin, Ethiopia using SWAT. Master's thesis, Indian Institute of Technology Roorkee. http://shodhbhagirathi.iitr.ac.in:8081/jspui/bitstream/123456789/16037/1/G29244.pdf

Belayneh M, Yirgu T, Tsegaye D (2019) Potential soil erosion estimation and area prioritization for better conservation planning in Gumara watershed using RUSLE and GIS techniques. Environ Syst Res 8:20. https://doi.org/10.1186/s40068-019-0149-x

Bewket W, Teferi E (2009) Assessment of soil erosion hazard and prioritization for treatment at the watershed level: case study in the Chemoga watershed, Blue Nile Basin, Ethiopia. Land Degrad Dev 20(6):609–622. https://doi.org/10.1002/ldr.944

Bogale A, Aynalem D, Adem A, Wolde M, Seifu T (2020) Spatial and temporal variability of soil loss in gully erosion in Upper Blue Nile Basin, Ethiopia. Appl Water Sci 10:106. https://doi.org/10.1007/s13201-020-01193-4

Borrelli P, Alewell C, Yang JE, Bezak N, Chen Y, Fenta AA, Fendrich AN, Gupta S, Matthews F, Modugno S, Haregeweyn N, Robinson DA, Tan F, Vanmaercke M, Verstraeten G, Vieira DCS, Panagos P (2023) Towards a better understanding of pathways of multiple co-occurring erosion processes on global cropland. Int Soil Water Conserv Res 11(4):713–725. https://doi.org/10.1016/j.iswcr.2023.07.008

Colman CB, Garcia KMP, Pereira RB, Shinma EA, Lima FE, Gomes AO, Oliveira PTS (2018) Different approaches to estimate the sediment yield in a tropical watershed. RBRH 23:e47. https://doi.org/10.1590/2318-0331.231820170178

Desmet PJJ, Govers G (1996) A GIS procedure for automatically calculating the USLE LS factor on topographically complex landscape units. J Soil Water Conserv 51(5):427–433

de Vente J, Poesen J, Verstraeten G, Van Rompaey A, Govers G (2008) Spatially distributed modelling of soil erosion and sediment yield at regional scales in Spain. Glob Planet Change 60(3–4):393–415. https://doi.org/10.1016/j.gloplacha.2007.05.002

Dile YT, Berndtsson R, Setegn SG (2013) Hydrological response to climate change for Gilgel Abay watershed. PLoS ONE 8(10): e79296. https://doi.org/10.1371/journal.pone.0079296

Durigon VL, Carvalho DF, Antunes MAH, Oliveira PTS, Fernandes MM (2014) NDVI time series for monitoring RUSLE cover management factor in a tropical watershed. Int J Remote Sens 35(2):441–453. https://doi.org/10.1080/01431161.2013.871081

Felix FC, Cândido BM, de Moraes JFL (2023) How suitable are vegetation indices for estimating the (R)USLE C-factor for croplands? A case study from Southeast Brazil. ISPRS Open J Photogramm Remote Sens 10:100050. https://doi.org/10.1016/j.ophoto.2023.100050

Ferro V, Porto P (2000) Sediment delivery distributed (SEDD) model. J Hydrol Eng 5(4):411–422. https://doi.org/10.1061/(ASCE)1084-0699(2000)5:4(411)

Gashaw T, Worqlul AW, Dile YT, Addisu S, Bantider A, Zeleke G (2020) Evaluating potential impacts of land management practices on soil erosion in the Gilgel Abay watershed, upper Blue Nile basin. Heliyon 6(8):e04777. https://doi.org/10.1016/j.heliyon.2020.e04777

Guzha AC, Rufino MC, Okoth S, Jacobs S, Nóbrega RLB (2018) Impacts of land use and land cover change on surface runoff, discharge and low flows: evidence from East Africa. J Hydrol Reg Stud 15:49–67. https://doi.org/10.1016/j.ejrh.2017.11.005

Haregeweyn N, Tsunekawa A, Nyssen J, Poesen J, Tsubo M, Tsegaye Meshesha D, Schütt B, Adgo E, Tegegne F (2015) Soil erosion and conservation in Ethiopia: a review. Prog Phys Geogr 39(6):750–774. https://doi.org/10.1177/0309133315598725

Hurni H (1985) Erosion–productivity–conservation systems in Ethiopia. In: Pla Sentis I (ed) Soil conservation and productivity. Proceedings of the 4th International Conference on Soil Conservation, Maracay, Venezuela, pp 654–674

Hurni K, Zeleke G, Kassie M, Tegegne B, Kassawmar T, Teferi E, Moges A, Tadesse D, Ahmed M, Degu Y, Kebebew Z, Hodel E, Amdihun A, Mekuriaw A, Debele B, Deichert G, Hurni H (2015) Economics of Land Degradation (ELD) Ethiopia case study. Soil degradation and sustainable land management in the rainfed agricultural areas of Ethiopia: an assessment of the economic implications. Report for the Economics of Land Degradation Initiative. https://www.eld-initiative.org

Jabar BS, Sayl KN, Alboresha R (2023a) Incorporating a GIS-based approach and SWAT model to estimate sediment in the western desert of Iraq. Int J Des Nat Ecodyn 18(4):791–800. https://doi.org/10.18280/ijdne.180405

Jabar BS, Sayl KN, Rashid RS (2023b) Approaches to modeling soil erosion caused by water: a review. AIP Conf Proc 2775(1):040001. https://doi.org/10.1063/5.0140870

Karydas CG, Panagos P (2016) Modelling monthly soil losses and sediment yields in Cyprus. Int J Digit Earth 9(8):766–787. https://doi.org/10.1080/17538947.2016.1156776

Ladegaard-Pedersen P, Sigsgaard C, Kroon A, Abermann J, Skov K, Elberling B (2017) Suspended sediment in a high-Arctic river: an appraisal of flux estimation methods. Sci Total Environ 580:582–592. https://doi.org/10.1016/j.scitotenv.2016.11.223

Lufafa A, Tenywa MM, Isabirye M, Majaliwa MJG, Woomer PL (2003) Prediction of soil erosion in a Lake Victoria basin catchment using a GIS-based Universal Soil Loss model. Agric Syst 76(3):883–894. https://doi.org/10.1016/S0308-521X(02)00012-4

Macedo PMS, Oliveira PTS, Antunes MAH, Durigon VL, Fidalgo ECC, de Carvalho DF (2021) New approach for obtaining the C-factor of RUSLE considering the seasonal effect of rainfalls on vegetation cover. Int Soil Water Conserv Res 9(2):207–216. https://doi.org/10.1016/j.iswcr.2020.12.001

Mahgoub M, Elalfy E, Soussa H, Abdelmonem Y (2024) Relation between the soil erosion cover management factor and vegetation index in semi-arid basins. Environ Earth Sci 83:337. https://doi.org/10.1007/s12665-024-11593-3

Maner SB (1958) Factors affecting sediment delivery rates in the Red Hills physiographic area. Trans Am Geophys Union 39(4):669–675. https://doi.org/10.1029/TR039i004p00669

McCool DK, Brown LC, Foster GR, Mutchler CK, Meyer LD (1987) Revised slope steepness factor for the Universal Soil Loss Equation. Trans ASAE 30(5):1387–1396. https://doi.org/10.13031/2013.30576

Morgan RPC (2005) Soil erosion and conservation, 3rd edn. Blackwell Publishing, Oxford. ISBN 9781405117814

Panagos P, Borrelli P, Meusburger K, Alewell C, Lugato E, Montanarella L (2015) Estimating the soil erosion cover-management factor at the European scale. Land Use Policy 48:38–50. https://doi.org/10.1016/j.landusepol.2015.05.021

Panagos P, Karydas C, Borrelli P, Ballabio C, Meusburger K (2023) Global soil erosion and land degradation assessment. Curr Opin Environ Sci Health 35:100492. https://doi.org/10.1016/j.coesh.2023.100492

Ren L, Han Z, Gao L, Zhang T, Wu R, Zhang H (2026) Advances in hyperspectral image unmixing: from algorithmic frameworks to practical applications. Inf Geogr 2(1):100035. https://doi.org/10.1016/j.infgeo.2025.100035

Renard KG, Foster GR, Weesies GA, McCool DK, Yoder DC (1997) Predicting soil erosion by water: a guide to conservation planning with the Revised Universal Soil Loss Equation (RUSLE). Agriculture Handbook No. 703. US Department of Agriculture, Washington, DC

Sayl K (2019) GIS and remote sensing-based approach for desert risk reduction. In: El-Askary HM, Lee S, Heggy E, Pradhan B (eds) Advances in remote sensing and geo informatics applications. Springer, Cham, pp 293–296. https://doi.org/10.1007/978-3-030-01440-7_67

Sayl KN, Yaman N, Abdulhameed IM, Khalaf HH (2026) Sustainable water management for agriculture to mitigate climate change effects. Water Resour Manag 40:100. https://doi.org/10.1007/s11269-026-04504-7

Shin GJ (1999) The analysis of soil erosion analysis in watershed using GIS. Ph.D. Dissertation, Department of Civil Engineering, Gang-won National University, Gangwon-do, South Korea.

Taye G, Poesen J, Van Wesemael B, Vanmaercke M, Teka D, Deckers J, Goosse T, Maetens W, Nyssen J, Hallet V, Haregeweyn N (2017) Determining RUSLE P- and C-factors for stone bunds and trenches in rangeland and cropland, North Ethiopia. Land Degrad Dev 28(2):632–642. https://doi.org/10.1002/ldr.2814

Tsegaye L, Bharti R (2021) Soil erosion and sediment yield assessment using RUSLE and GIS-based approach in Anjeb watershed, Northwest Ethiopia. SN Appl Sci 3:582. https://doi.org/10.1007/s42452-021-04564-x

Usman K., Deribew KT, Alemu G, Hailu S (2023) Spatial modeling of soil loss as a response to land use-land cover change in the Limu-Seqa watershed, Western Highlands of Ethiopia. Heliyon 9(3): e14590. https://doi.org/10.1016/j.heliyon.2023.e14590

Van der Knijff JM, Jones RJA, Montanarella L (2000) Soil erosion risk assessment in Europe. EUR 19044 EN. European Soil Bureau, Joint Research Centre, European Commission, Office for Official Publications of the European Communities, Luxembourg

Vanoni VA (ed) (1975) Sedimentation engineering. ASCE Manuals and Reports on Engineering Practice No. 54. American Society of Civil Engineers, New York

Vîrghileanu M, Șandric I, Mihai B-A, Săvulescu I, Bizdadea C-G (2026) Comparative assessment of vegetation cover and management factor in soil loss modelling using Sentinel-2 MSI time-series imagery: a case study from the Romanian Carpathian-Subcarpathian region. Remote Sens Appl Soc Environ 42:102013. https://doi.org/10.1016/j.rsase.2026.102013

Walling DE (1983) The sediment delivery problem. J Hydrol 65(1–3):209–237. https://doi.org/10.1016/0022-1694(83)90217-2

Williams JR, Berndt HD (1972) Sediment yield computed with universal equation. J Hydraul Div 98(12):2087–2098. https://doi.org/10.1061/JYCEAJ.0003498

Wischmeier WH, Smith DD (1978) Predicting rainfall erosion losses: a guide to conservation planning. Agriculture Handbook No. 537. US Department of Agriculture, Washington, DC

Woldemariam A, Getachew T, Chanie T (2023) Long-term trends of river flow, sediment yield and crop productivity of Andit Tid watershed, central highland of Ethiopia. All Earth 35(1):3–15. https://doi.org/10.1080/27669645.2022.2154461

Worku KB, Zimale FA, Francke T, Zargar M, Bronstert A (2026) Machine learning-based sedigraph reconstruction for enhanced sediment yield estimation in the Upper Blue Nile Basin. EarthArXiv preprint. https://doi.org/10.31223/X5BV38

Yousefi S, Jaafari A, Valjarević A, Gomez C, Keesstra S (2022) Vulnerability assessment of road networks to landslide hazards in a dry-mountainous region. Environ Earth Sci 81:22. https://doi.org/10.1007/s12665-022-10650-z

Zerihun M, Mohammedyasin MS, Sewnet D, Adem AA, Lakew M (2018) Assessment of soil erosion using RUSLE, GIS and remote sensing in NW Ethiopia. Geoderma Reg 12:83–90. https://doi.org/10.1016/j.geodrs.2018.01.002

Zhang H, Yang Q, Li R, Liu Q, Moore D, He P, Ritsema CJ, Geissen V (2013) Extension of a GIS procedure for calculating the RUSLE equation LS factor. Comput Geosci 52:177–188. https://doi.org/10.1016/j.cageo.2012.09.027

Acknowledgements

The author gratefully acknowledges the Head of the Department of Earth Sciences and the President of the University of Gondar, Dr. Desalegne Mengesha, for providing the facilities to conduct this study. The author also thanks the U.S. Geological Survey (USGS) EarthExplorer for the satellite datasets, Ethiopian Meteorological Institute (EMI), Gondar for the meteorological data, and the Soil and Water Resources Department of Ethiopia for the sediment and discharge records (secondary data). The author is grateful to the staff members who assisted with field data collection.

Funding

The author declares that no funds, grants, or other support were received during the preparation of this manuscript.

Author Contributions

Balabathina Veera Narayana: conceptualization, methodology, formal analysis, investigation, data curation, visualization, writing – original draft, writing – review and editing. The sole author read and approved the final manuscript.

Ethical Approval

Not applicable. This study did not involve human participants or animals.

Consent to Participate

Not applicable.

Consent to Publish

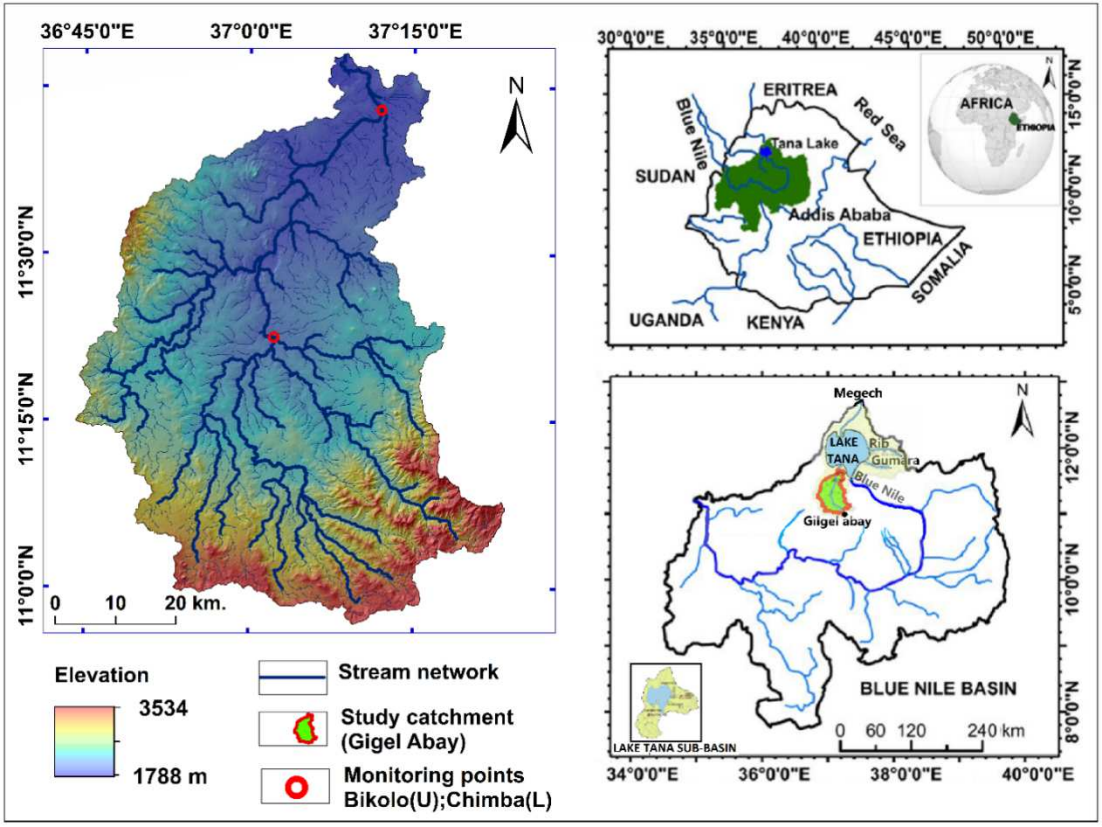
Not applicable.

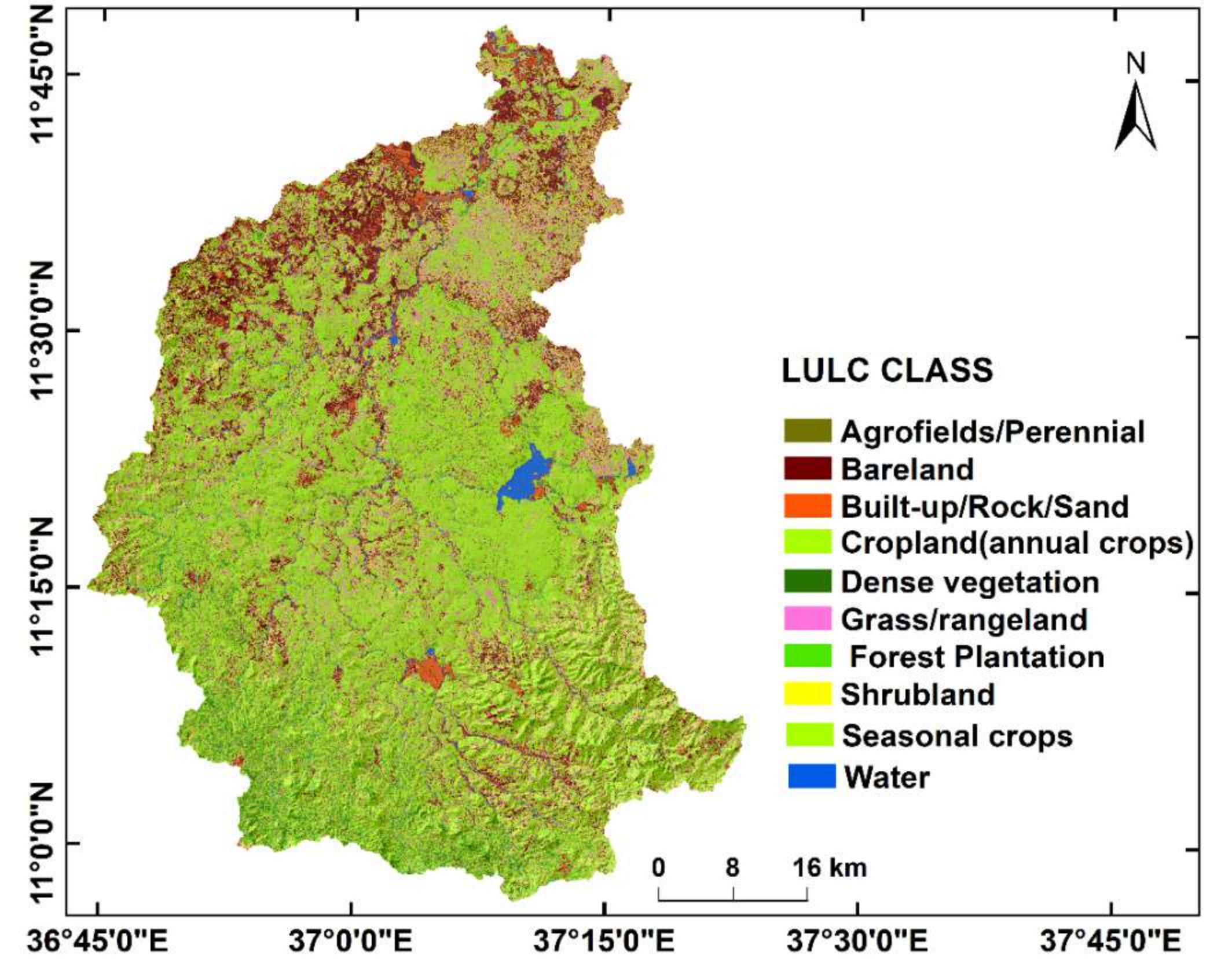
Competing Interests

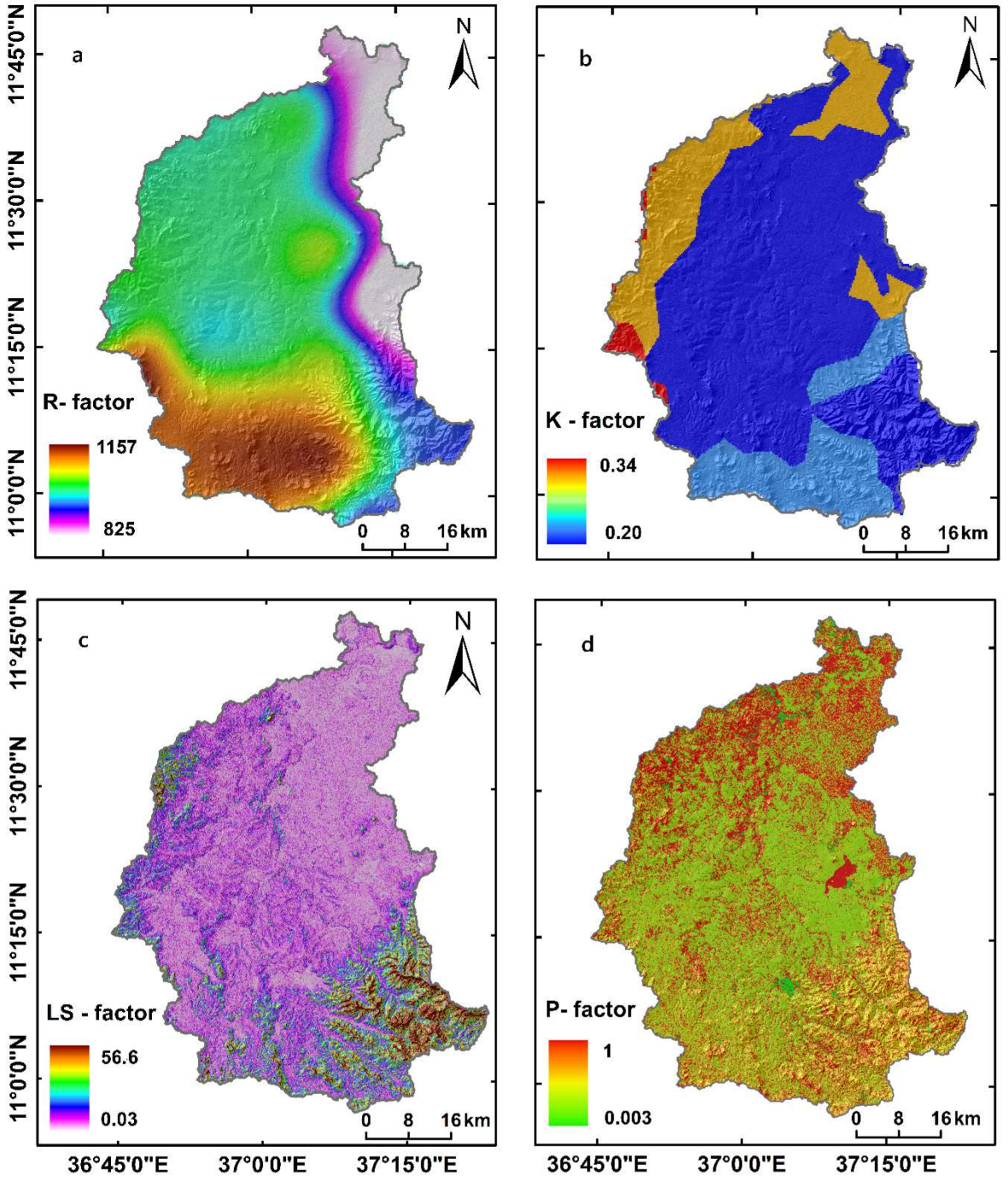
The author declares no competing interests.

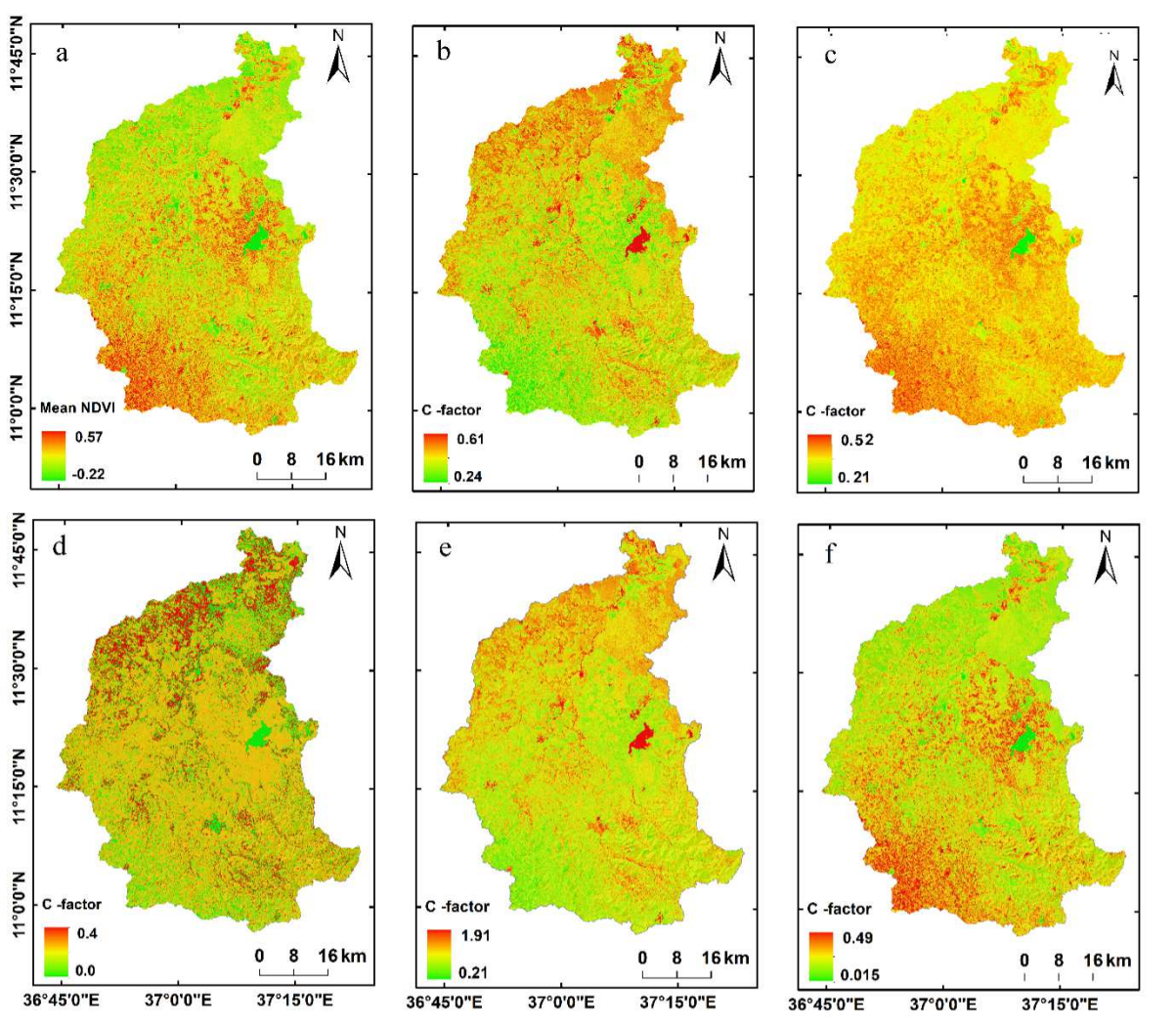
Data Availability Statement

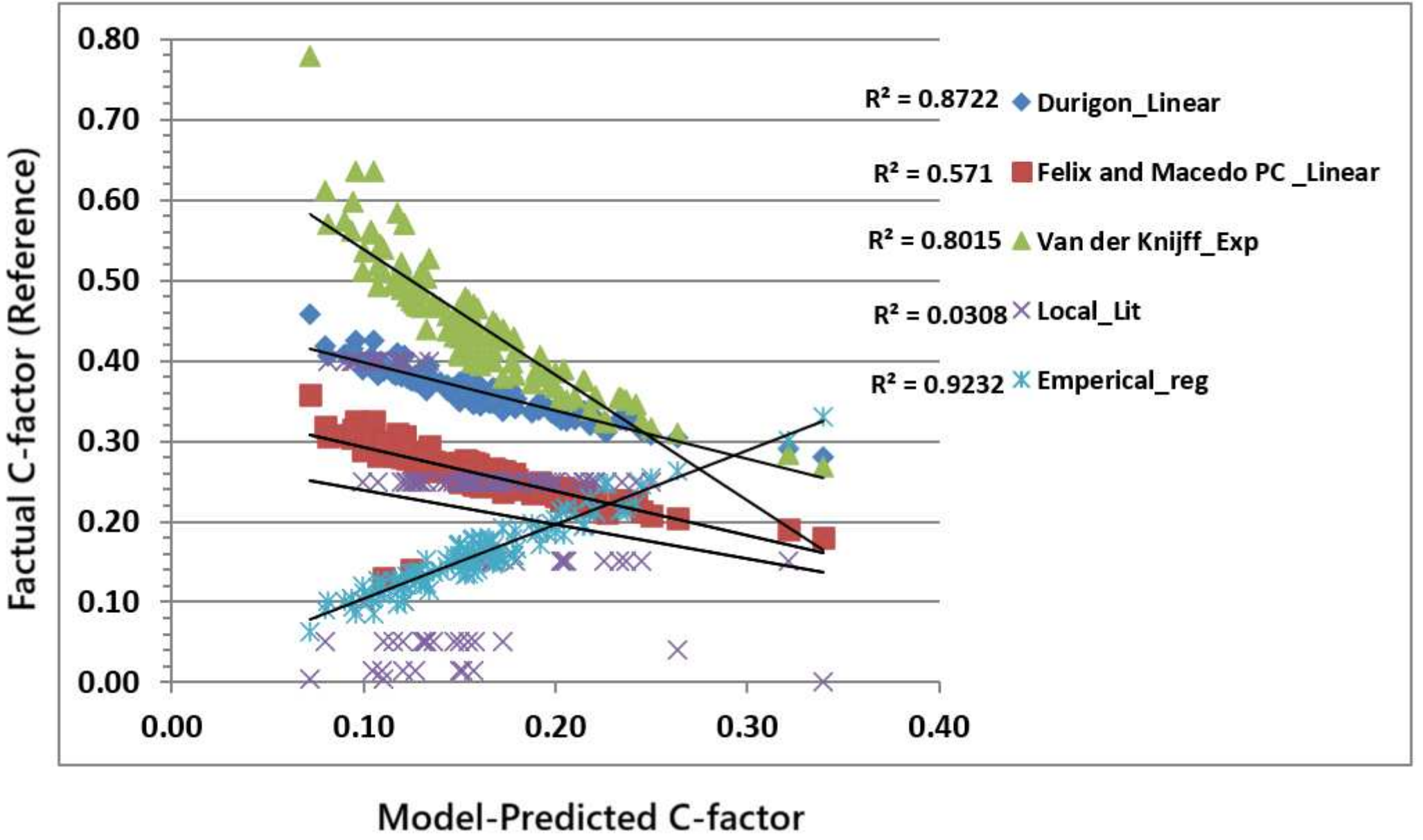
The datasets generated and analysed during this study (processed RUSLE factor layers, C-factor and soil-loss scenario rasters, sediment delivery ratio layers, the land-use/land-cover map, field-calibration data, summary sediment-gauge data, and source data for all tables and figures) are available from the corresponding author upon reasonable request. Landsat 8 OLI imagery is available from USGS EarthExplorer (https://earthexplorer.usgs.gov), ASTER GDEM data form LP DAAC, NASA and the Harmonized World Soil Database (HWSD v1.2) is available from FAO. The source of the soils, rainfall and historical mean NDVI data are the secondary data used for this study.

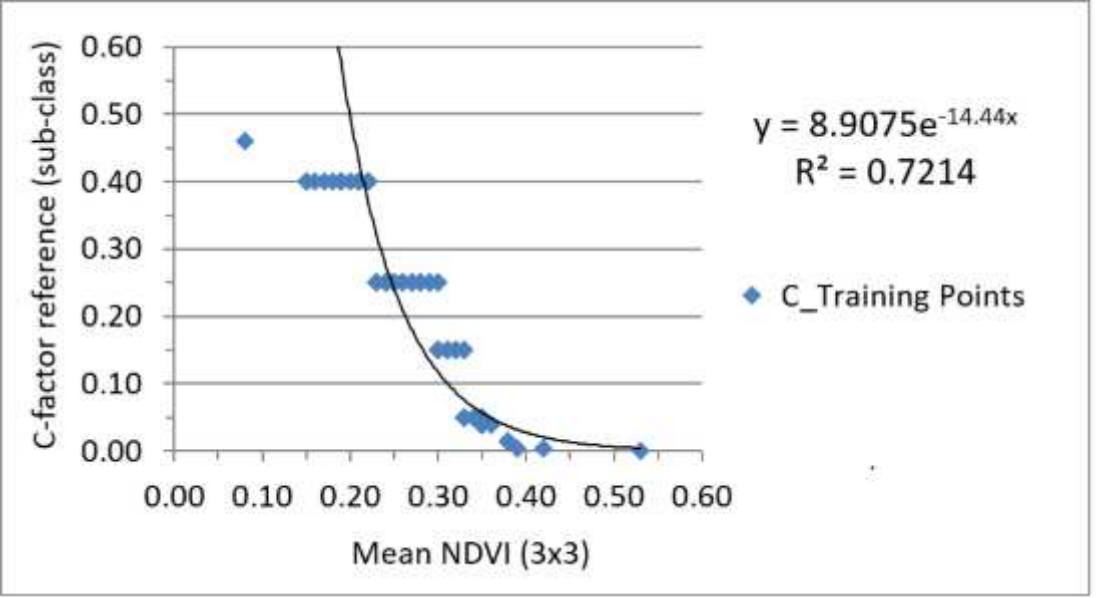

36°45'0"E
37°0'0"E
37°15'0"E
11°30'0"N
11°15'0"N
11°0'0"N
N
0 10 20 km.
Elevation
3534
1788 m
Stream network
Study catchment (Gigel Abay)
Monitoring points Bikolo(U);Chimba(L)
30°0'0"E
35°0'0"E
40°0'0"E
45°0'0"E
50°0'0"E
15°0'0"N
10°0'0"N
5°0'0"N
ERITREA
Red Sea
Blue Nile
Tana Lake
SUDAN
Addis Ababa
ETHIOPIA
SOMALIA
UGANDA
KENYA
AFRICA
ETHIOPIA
Megech
LAKE TANA
Rib
Gumara
Blue Nile
Gilgel abay
BLUE NILE BASIN
LAKE TANA SUB-BASIN
0 60 120 240 km
34°0'0"E
36°0'0"E
38°0'0"E
40°0'0"E
12°0'0"N
10°0'0"N
8°0'0"N

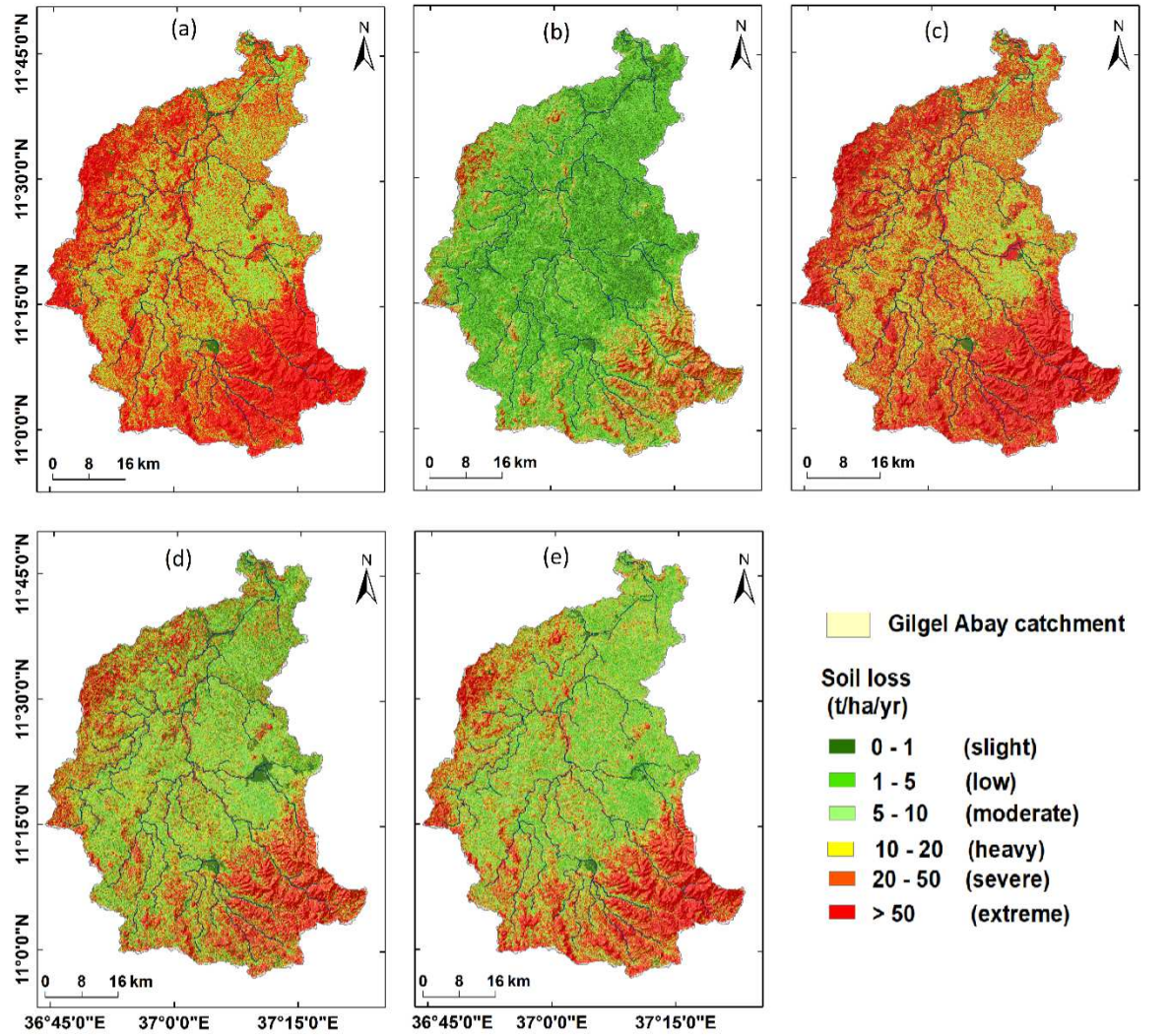

11°45'0"N
11°30'0"N
11°15'0"N
11°0'0"N
36°45'0"E
37°0'0"E
37°15'0"E
37°30'0"E
37°45'0"E
N
LULC CLASS
Agrofields/Perennial
Bareland
Built-up/Rock/Sand
Cropland(annual crops)
Dense vegetation
Grass/rangeland
Forest Plantation
Shrubland
Seasonal crops
Water
0
8
16 km

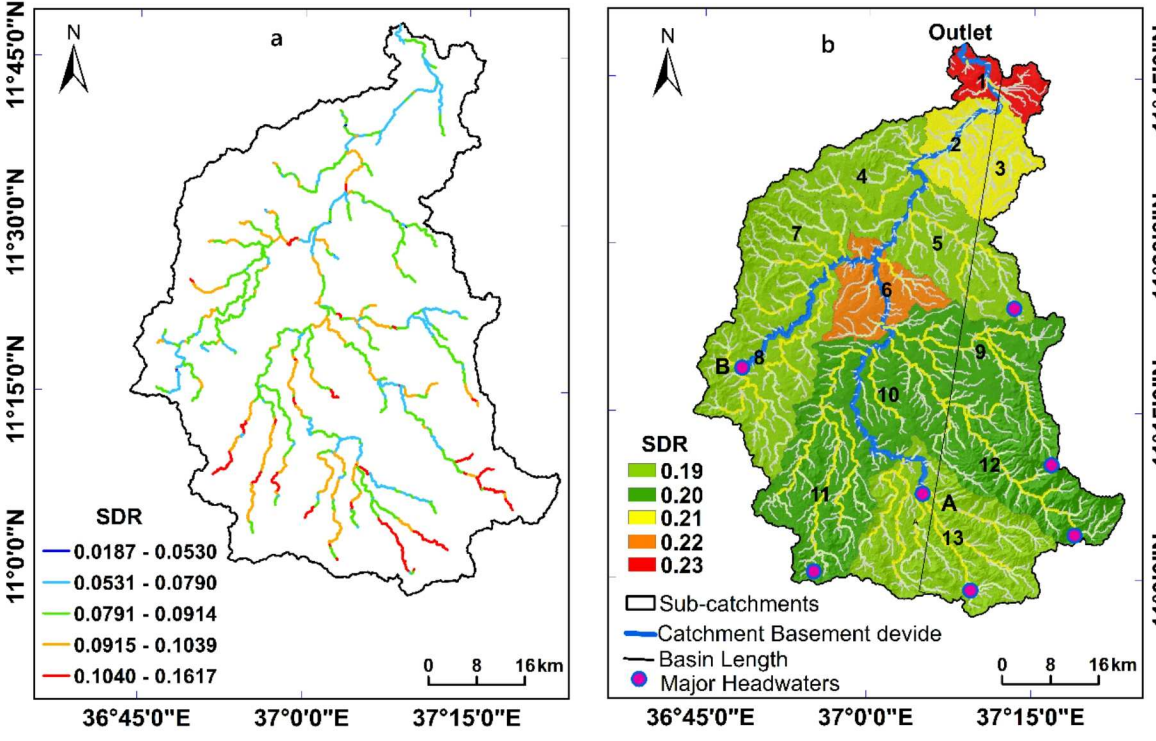

a
N
R- factor
1157
825
0 8 16 km
b
N
K - factor
0.34
0.20
0 8 16 km
c
N
LS - factor
56.6
0.03
0 8 16 km
d
P- factor
1
0.003
0 8 16 km
11°45'0"N
11°30'0"N
11°15'0"N
11°0'0"N
36°45'0"E
37°0'0"E
37°15'0"E

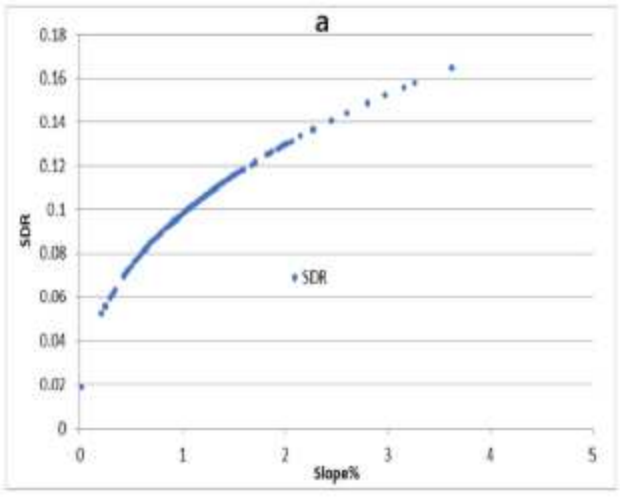

a
N
Mean NDVI
0.57
-0.22
0 8 16 km
b
N
C -factor
0.61
0.24
0 8 16 km
c
N
C -factor
0.52
0. 21
0 8 16 km
d
N
C -factor
0.4
0.0
0 8 16 km
e
N
C -factor
1.91
0.21
0 8 16 km
f
N
C -factor
0.49
0.015
0 8 16 km
11°45'0"N
11°30'0"N
11°15'0"N
11°0'0"N
36°45'0"E
37°0'0"E
37°15'0"E

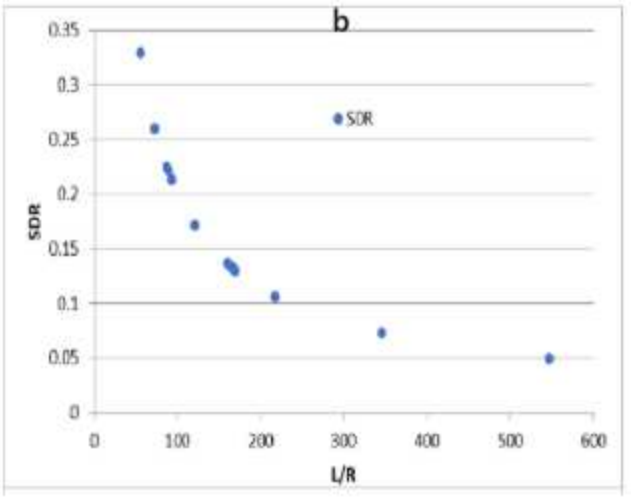

0.80
0.70
0.60
0.50
0.40
0.30
0.20
0.10
0.00
Factual C-factor (Reference)
0.00
0.10
0.20
0.30
0.40
Model-Predicted C-factor
R² = 0.8722
Durigon_Linear
R² = 0.571
Felix and Macedo PC _Linear
R² = 0.8015
Van der Knijff_Exp
R² = 0.0308
Local_Lit
R² = 0.9232
Emperical_reg

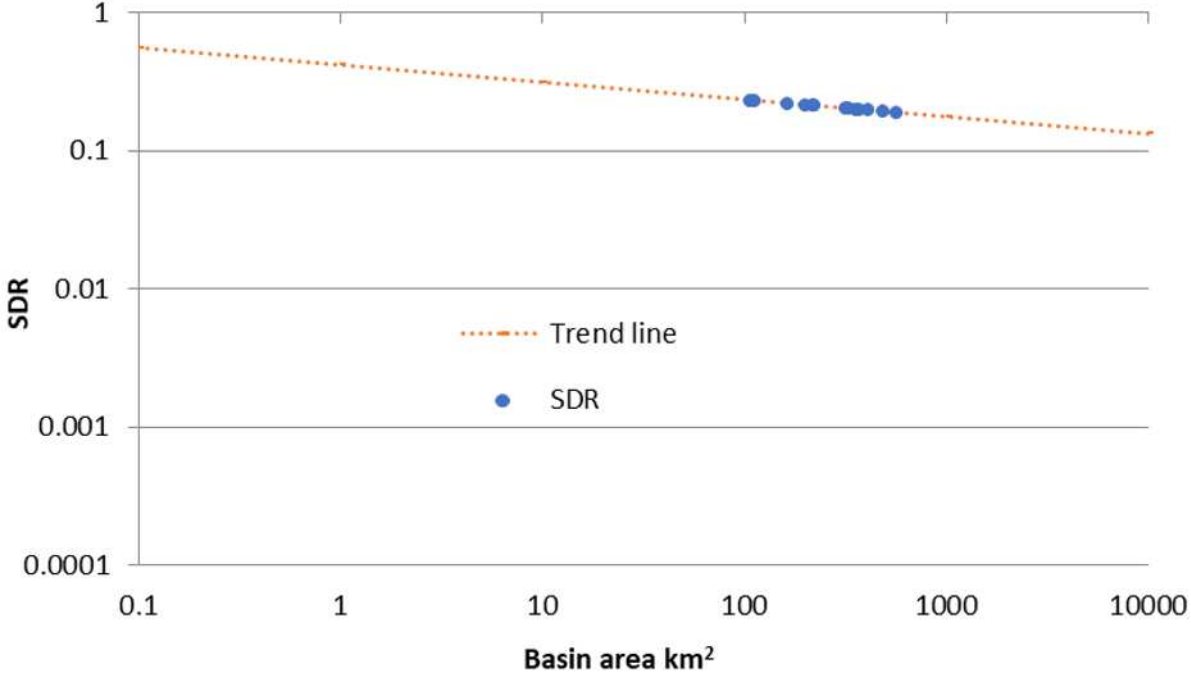

C-factor reference (sub-class)
0.60
0.50
0.40
0.30
0.20
0.10
0.00
0.00 0.10 0.20 0.30 0.40 0.50 0.60
Mean NDVI (3x3)
y = 8.9075e-14.44x
R² = 0.7214
C_Training Points


(a)
(b)
(c)
(d)
(e)
N
0 8 16 km
11°45'0"N
11°30'0"N
11°15'0"N
11°0'0"N
36°45'0"E
37°0'0"E
37°15'0"E
Gilgel Abay catchment
Soil loss
(t/ha/yr)
0 - 1 (slight)
1 - 5 (low)
5 - 10 (moderate)
10 - 20 (heavy)
20 - 50 (severe)
> 50 (extreme)


a
N
SDR
0.0187 - 0.0530
0.0531 - 0.0790
0.0791 - 0.0914
0.0915 - 0.1039
0.1040 - 0.1617
0 8 16km
11°45'0"N
11°30'0"N
11°15'0"N
11°0'0"N
36°45'0"E
37°0'0"E
37°15'0"E
b
N
Outlet
1
2
3
4
5
6
7
8
9
10
11
12
13
A
B
SDR
0.19
0.20
0.21
0.22
0.23
Sub-catchments
Catchment Basement devide
Basin Length
Major Headwaters
0 8 16km
11°45'0"N
11°30'0"N
11°15'0"N
11°0'0"N
36°45'0"E
37°0'0"E
37°15'0"E


a
SDR
Slope%
SDR
0.18
0.16
0.14
0.12
0.1
0.08
0.06
0.04
0.02
0
0
1
2
3
4
5


b
SDR
L/R
SDR
0.35
0.3
0.25
0.2
0.15
0.1
0.05
0
0
100
200
300
400
500
600


1
0.1
0.01
0.001
0.0001
SDR
Trend line
SDR
0.1
1
10
100
1000
10000
Basin area km2

Supplementary Files

This is a list of supplementary files associated with this preprint. Click to download.

- Supplementarymaterial.docx